Stereotyped behavioral maturation and rhythmic quiescence in *C. elegans* embryos

Evan L. Ardiel
Department of Molecular Biology
Massachusetts General Hospital
Boston, MA, 02114, USA
Department of Neurobiology
Harvard Medical School
Boston, MA, 02115, USA
ardiel@molbio.mgh.harvard.edu

Andrew Lauziere
Laboratory of High Resolution Optical Imaging
National Institutes of Health
Bethesda, MD, 20814, USA
Department of Mathematics
University of Maryland, College Park
College Park, MD 20742
lauziere@umd.edu

Stephen Xu
Laboratory of High Resolution Optical Imaging
National Institutes of Health
Bethesda, MD, 20814, USA
stephen.xu.42@gmail.com

Brandon J. Harvey
Laboratory of High Resolution Optical Imaging
National Institutes of Health
Bethesda, MD, 20814, USA
Department of Neurology, Emory University
Atlanta, GA, 30322, USA

Stephen Nurrish
Department of Molecular Biology
Massachusetts General Hospital
Boston, MA, 02114, USA
Department of Neurobiology
Harvard Medical School
Boston, MA, 02115, USA

Joshua M. Kaplan
Department of Molecular Biology
Massachusetts General Hospital
Boston, MA, 02114, USA
Department of Neurobiology
Harvard Medical School
Boston, MA, 02115, USA

Hari Shroff
Laboratory of High Resolution Optical Imaging
National Institutes of Health
Bethesda, MD 20892
hari.shroff@nih.gov

July 19, 2022

ABSTRACT

Systematic analysis of rich behavioral recordings is being used to uncover how circuits encode complex behaviors. Here we apply this approach to embryos. What are the first embryonic behaviors and how do they evolve as early neurodevelopment ensues? To address these questions, we present a systematic description of behavioral maturation for *Caenorhabditis elegans* embryos. Posture libraries were built using a genetically encoded motion capture suit imaged with light-sheet microscopy and annotated using custom tracking software. Analysis of cell trajectories, postures, and behavioral motifs revealed a stereotyped developmental progression. Early movement is dominated by flipping between dorsal and ventral coiling, which gradually slows into a period of reduced motility. Late-stage embryos exhibit sinusoidal waves of dorsoventral bends, prolonged bouts of directed motion, and a rhythmic pattern of pausing, which we designate slow wave twitch (SWT). Synaptic transmission is required for late-stage motion but not for early flipping nor the intervening inactive

phase. A high-throughput behavioral assay and calcium imaging revealed that SWT is elicited by the rhythmic activity of a quiescence-promoting neuron (RIS). Similar periodic quiescent states are seen prenatally in diverse animals and may play an important role in promoting normal developmental outcomes.

1 Introduction

The set of synaptic connections assembled during development form a physical substrate for brain activity, behavior, and cognition. Diverse model systems have been deployed to identify the molecular components essential for initiating this process, from neuronal differentiation to synaptogenesis. In parallel, postnatal behaviors have been studied from genes to cells to circuits. By comparison, few datasets probe the earliest emergence of functional neural circuitry. New principles are likely to be discovered through focused analysis of nascent neuronal circuits and the behaviors they elicit. Indeed, the structural remodeling of synapses peaks early and becomes less dynamic with age and the maturation of some circuitry is restricted to specific stages (critical periods) early in development [1].

In 1695, Antonie van Leeuwenhoek expressed his amazement at first seeing motility in unborn mussels, writing that the graceful rotations were beyond comprehension [2]. Careful observation has since uncovered details of embryonic behavior across phylogeny. Studies of the chick embryo were particularly influential. Here it was established that rhythmic motility was mediated by stereotyped spontaneous activity in neuromuscular circuitry [3]. Behavioral classification has traditionally relied on expert observers; however, new tools for data-driven analysis of rich behavioral recordings are accelerating progress in ethology and systems neuroscience [4, 5, 6, 7]. Applying these tools to embryos has the potential to illuminate how the brain assumes control of motor output. What are the first behaviors that embryos exhibit? Is there a stereotyped developmental progression for embryonic behaviors? Is this progression dictated by the timing of ongoing neurodevelopment (i.e., circuit wiring)? Do embryonic circuits encode behaviors by mechanisms distinct from those found in mature, post-natal circuits?

To begin addressing these questions, here we build a comprehensive picture of embryonic behavior in the microscopic roundworm *Caenorhabditis elegans*. *C. elegans* offers several advantages for investigating the emergence of functional neuronal circuitry and behavior. Embryos are small ($\approx 50x30x30\mu m^3$) and transparent, enabling in vivo imaging of cell migration, neurite growth, synaptogenesis, neuronal activity, and behavior during the mere $\approx$14 hours from fertilization to hatching [8, 9, 10, 11, 12, 13, 14, 15, 16, 17, 18, 19]. In addition, *C. elegans* boasts a sophisticated molecular genetic toolkit, a complete neuronal wiring diagram, and a comprehensive atlas of single cell gene expression across embryogenesis [20, 21, 22, 23]. *C. elegans* has proven a powerful system for analyzing circuits and behavior; however, virtually all such studies have focused on post-embryonic stages, including "cradle to grave" behavioral recordings [24, 25]. In embryos, cell movement has been fully tracked from the first cell division up to the first muscle contraction, which occurs at about 430 minutes post-fertilization (mpf) [26, 27, 28]. Tracking behavior beyond this point is complicated by the embryo's rapid movements and entangled body postures. At hatching, the 222-cell larval nervous system already supports directed locomotion and even learning and memory [29]. Thus, a functional motor program emerges over what is arguably the least documented 6 hours of the worm's life (430-800 mpf).

When the nervous system begins generating behavior is currently unknown. Pre-synaptic proteins are first localized in the worm's "brain", a large circumferential bundle of axons called the nerve ring, less than an hour before the first muscle contraction [14]. However, these pre-synaptic proteins exhibit high diffusional mobility at this stage [14] and it is unclear when nerve ring synapses become functional. Mutants lacking essential muscle genes arrest as two-fold embryos, indicating that muscle contractions are required for elongation of the embryo's body [30]. Elongation is unaffected in mutants deficient for neuronal function, implying that initial muscle contractions do not require neuronal input. In a developmental series of electron micrographs, pre-synaptic vesicle clusters at body wall neuromuscular junctions are first observed a couple of hours after the onset of movement ($\approx$550 mpf) [31]. In late-stage embryos, backward locomotion correlates with activity of backward command interneurons [16], suggesting the existence of a functional motor program prior to hatching. Here we documented all postural transitions for the final few hours of embryogenesis (530 mpf to hatching). We find that embryos exhibit a stereotyped pattern of behavioral maturation, including a period of rhythmic quiescence. This rhythmic quiescence is elicited by the RIS neuron, which promotes sleep-like behaviors in larvae and adults [32, 33]. Rhythmic sleep-like states are a highly conserved feature of prenatal behavior in other animals [34, 35, 36, 37, 38]. *C. elegans* offers a powerful system for investigating this phenomenon.

2 Results

2.1 Building embryo posture libraries

Building posture libraries to investigate embryo behavior proved challenging for several reasons. First, embryos are susceptible to photodamage, requiring us to carefully calibrate illumination dose, acquisition speed, spatial resolution, and signal-to-noise ratio. Second, at the low illumination dose required for sustained embryo imaging, fluorescent labels used to visualize posture are dim, necessitating optimized segmentation schemes to detect them. Third, the segmented labels must be tracked accurately, a task complicated by imperfect cell detections and abrupt embryo movements.

To assess posture, we imaged ten pairs of skin cells (termed seam cells) that run along the left and right sides of the *C. elegans* embryo. We defined posture as the joint identification of all seam cell nuclei in an image volume. Seam cells expressing nuclear localized GFP were imaged by light-sheet fluorescence microscopy, which allows rapid optical sectioning with minimal photodamage. With single view imaging (iSPIM) [39, 40], we recorded volumes at 3 Hz for more than 4.5 hours (Fig. 1a, b, Fig. 1-Video 1). Imaging did not affect the timing of the Q/V5 cell division ($\approx$695-725 mpf) nor hatching (¡820 mpf) and did not induce detectable photobleaching. Consequently, we conclude that this imaging protocol did not interfere with normal embryonic development.

To track posture, seam cell nuclei must first be accurately detected (i.e., distinguished from each other and background). Using image volumes with manually annotated seam cells, we compared the performance of several image segmentation methods. The best performance was obtained using a 3D convolutional neural network [41, 42], although the Laplacian of Gaussians [43, 44, 45], a traditional method for blob detection, achieved the same level of precision with only a slightly lower recall across the test set (Table 2).

After detection, we evaluated methods for enabling comprehensive tracking of nuclear locations across all image volumes. Different multiple object tracking (MOT) methods trade computational complexity for modeling capability [46]. The first, and simplest, MOT strategy considered was the Global Nearest Neighbor (GNN) method. In GNN, nuclei are treated as independent objects, and are tracked by minimizing frame-to-frame object displacement. However, GNN often failed when nuclear trajectories intersected or when the detection set contained false positives, coordinates erroneously counted as nuclei centers. GNN can be augmented to improve performance. For example, dynamical physical modeling (e.g., Kalman Filtering; Kalman, 1960) can be incorporated to predict object trajectories. Multiple hypothesis tracking (MHT) [47, 48, 49] leverages this strategy and considers multiple future frames to distinguish between competing object assignments in the current frame. MHT is considered a state-of-the-art MOT method; however, MHT is most effective when imaging is rapid enough that object trajectories appear smooth. Unfortunately, for late-stage embryos, a volumetric imaging rate of 3 Hz (selected to preserve embryo health) does not reliably produce smooth trajectories.

Seam cells have fixed anatomical positions that define a flexible lattice. This anatomical constraint causes seam cells to move in a correlated manner. We reasoned that MHT could be improved by incorporating these correlations. To test this idea, we developed Multiple hypothesis hypergraph tracking (MHHT) [50]. MHHT extends MHT by using empirically derived covariances (Fig. 1c) to compute the cost of competing cell assignment hypotheses. MHHT also excludes hypotheses that generate physically impossible body contortions (i.e., body segments passing through one another). MHHT then identifies the cost minimizing posture of K sampled hypotheses over N future frames (Fig. 1d). MHHT should improve tracking compared to strategies where nuclei are assumed to move independently.

To compare the efficacy of MHHT to simpler tracking models, we performed simulations on a test embryo (51,533 image volumes) for which seam cell positions were manually annotated. Using the annotated nuclear locations, MHHT (K=5, N=5) incorrectly assigned at least one seam cell (and thus misidentified posture) in 1.43% of image volumes, which was significantly less than the error rate obtained with GNN tracking (2.01% of volumes, K=1, N=1, $p < 5.1e - 13$). Higher error rates were observed when seam cells were detected using the modified 3D U-Net; however, MHHT (5.25% of volumes, K=25, N=2) still outperformed GNN (5.88% of volumes, K=1, N=1, $p < 1.02e - 5$). MHHT also has a feature designed to anticipate tracking failures. When the lowest assigned cost crosses a user-defined threshold, MHHT prompts the user to manually edit cell assignments before resuming automated tracking. The MHHT code is freely available at `https://github.com/lauziere/MHHT`.

Collectively, these methods (iSPIM, 3D U-Net segmentation, and MHHT) comprise a semi-automated pipeline for documenting embryo postures. Using these methods, we generated a comprehensive catalogue of postural transitions for three control embryos, recording the position of all seam cells three times per second from 530 mpf to hatch (¿4.5 hours). These 150,000+ annotated image volumes (freely available on FigShare, `https://figshare.com/s/6d498d74f98cca447d41`)) create a new resource for the systematic analysis of *C. elegans* embryo behavior.

2.2 Assessing speed, direction of motion, and bout durations

Next, we used a variety of analytical approaches to quantify embryo motion. Mean squared displacement (MSD) is commonly used to describe the motion of particles and cells. Consistent with confined motion, MSD of embryonic seam cell nuclei saturated in minutes. Anterior seam cells had the highest MSD plateaus, which approximated the square of the egg's mean radius (Fig. 2a). These results demonstrate that the embryo's anterior end explored the full eggshell volume. A "diffusion coefficient" (D) for each seam cell nucleus was estimated by linear fitting over 10 seconds (i.e., 30 frames). This analysis revealed that anterior seam cell motility was greater than that exhibited by posterior cells (Fig. 2b). We also observed a consistent developmental shift, with the least motility occurring at ≈600 mpf (Fig. 2c). Fig. 2d illustrates the developmental transitions of two seam cells. As predicted from their MSD (Fig.2a), H1 (an anterior cell) explores the full extent of the eggshell, while V6 (a posterior cell) is more confined. The H1 "diffusion coefficient" was virtually identical at 530 and 750 mpf; however, the later trajectory reveals a shift to more directed movement, indicating more mature embryonic behavior.

To further characterize embryo behavior, we considered speed and movements along the anteroposterior axis. For embryo speed, we measured displacement of left-right seam cell pair midpoints (H1 to V5) over 1 second (3 frames), and then calculated a weighted average based on the straight-line length of the body at that segment and volume (Fig. 2e). Embryo speed varied with age, mirroring the developmental shift in seam cell diffusion coefficients described above (Fig. 2c, e). A marked increase in the coefficient of variation of embryo speed highlights the extent to which movement becomes increasingly punctuated in the final hours of embryogenesis (Fig. 2e, f), exhibiting both big displacements and periods of relative inactivity. Timing movements along the anteroposterior axis, we found that the duration of both forward and backward bouts increased over the final two hours of embryogenesis, as did the duration of pausing (Fig. 2e, g). In summary, seam cell tracking reveals a consistent developmental progression in embryo behavior. Immature embryos move nearly continuously in short trajectories, while mature embryos show prolonged bouts of forward and backward movement punctuated with pausing.

2.3 A high-throughput assay for assessing embryonic twitching

Seam cell tracking has two potential limitations as a strategy to analyze embryo behavior. First, the fluorescence imaging required for posture tracking could artificially distort the observed embryonic behaviors (e.g., due to subtle phototoxic effects). Second, although our imaging pipeline is semi-automated, seam cell tracking remains labor intensive. To address these concerns, we devised an independent high throughput brightfield assay to assess overall embryonic motility. Brightfield images of up to 60 embryos were simultaneously acquired at 1 Hz, and frame-to-frame changes in pixel intensity were used as a proxy for embryo movement (Fig. 3a, Fig. 3-Video 1). The resulting twitch profiles were highly stereotyped, exhibiting three salient phases: an immature active phase (≈450-550 mpf), followed by a relatively inactive period (≈550-650 mpf), followed by a second active phase (≥650 mpf; Fig 3b) with a broadened distribution of movement magnitudes (Fig. 3c). We generated scalograms to visualize the temporal structure of twitch profiles over a range of timescales. This analysis revealed a prominent feature in the 20-40 mHz frequency band, occurring about an hour before hatching (Fig. 3d). This feature was attributed to an increased propensity for prolonged pausing, as had been seen in seam cell tracks at this stage (Fig. 2g). We call this behavioral signature slow wave twitch (SWT).

While the general pattern of behavioral maturation was highly stereotyped, absolute timings of the different phases varied between experiments. For example, the mean time from first twitch to hatch ranged from 4.5 to 6.5 hours (324.1 +/- 37.0 minutes, mean +/- SEM) across 31 brightfield recordings (Fig.3-Supp. 1). This variability could result from differences in temperature or buffer salinity, both of which have been shown to influence the rate of development [51, 18]. The poly-L-lysine used for sticking embryos to the coverslip is an additional potential source of variability. However, the timing of SWT scaled with hatch time (Fig.3-Supp. 1), suggesting that the relative timing of development was consistent across experiments. In summary, similar motion profiles were observed in the brightfield and seam cell tracking assays, further suggesting that the observed progression of behaviors is an authentic feature of embryonic development.

2.4 Eigen-embryos compactly describe posture and behavioural motifs

Adult worms crawling on a 2D agar surface explore a low dimensional postural space. A prior study showed that over 90% of variance in dorsoventral bending along the midline could be accounted for with just 4 principal components (PCs), which were termed "eigenworms" [52]. To describe embryo posture, we used seam cell positions to fit each side of the body with a natural cubic spline and then computed dorsoventral bending angles between adjacent seam cells (totalling 18 bend angles in each volume; Fig. 4a, b). Four PCs captured approximately 88% of variation in the 18 angles (Fig. 4c, d). The corresponding eigenvectors of the four leading components (termed eigen-embryos)

were stereotyped between animals. For example, PC1 captures ventral or dorsal coiling (i.e., all ventral or all dorsal body bends, respectively) while PC2 describes postures with opposing anterior and posterior bends (Fig. 4e). In this framework, embryonic posture can be approximated by a linear combination of eigen-embryos. The contribution of eigen-embryos shifted consistently across development, with less variance accounted for by PC1 as PC2 and PC3 gained prominence (Fig. 4d). PC2 and PC3 approximate sinusoids with a phase difference of about 90° that can be combined to generate travelling waves of dorsoventral bending. The developmental shift towards PC2 and PC3 more closely approximates the adult motion pattern, where the top two PCs also describe sinusoids with a 90° phase shift [52]. The relatively limited dimensionality of dorsoventral bending observed in both adults and embryos is likely a consequence of muscle anatomy, with electrically coupled muscle bundles running ventrally and dorsally along the body [20].

Because seam cells are bilaterally symmetric, we could not assign left versus right identity and consequently could not distinguish dorsal from ventral bends. At hatching, dorsal and ventral muscles are controlled by distinct classes of motor neurons [53, 54, 55]. We wondered if this difference in connectivity results in a systematic asymmetry in embryo postures. Consistent with this idea, we observed an asymmetry in the PC1 amplitude distribution of late-stage embryos (Fig. 4-Supp. 1a). To determine if the bias was consistently dorsal or ventral, we acquired a supplemental dataset of 16 embryos expressing additional fluorescent markers. The added markers allowed us to unambiguously identify left and right seam cell nuclei by manual inspection. This supplemental dataset was collected at lower temporal resolution (5 min intervals), thereby precluding detailed behavioral tracking. The postures exhibited by embryos in the supplemental dataset were described by a similar set of eigen-embryos as the original dataset (Fig. 4-Supp. 1c). In the final hours of embryogenesis, the postures in the supplemental dataset exhibited a dorsal bias (Fig. 4-Supp. 1b). By assuming a dorsal bias for the original dataset, we were able to distinguish left and right seam cells (and consequently dorsal and ventral body bends) in the three embryos recorded at 3 Hz.

Our analysis of embryo postures is consistent with a prior study of embryo behavior [17]. Using only differential interference contrast (DIC) microscopy and manual visual inspection, this study describes embryo motion as flips about the anteroposterior axis that decline in frequency ahead of the emergence of the "larval locomotor pattern." This proposed developmental progression was readily apparent in posture space. Flips about the anteroposterior axis were seen as oscillating PC1 amplitudes, which signifies alternating dorsal and ventral coiling (Fig. 4f; Fig. 4-Supp. 2a, b). The "larval locomotor pattern" was best captured by PC2 and PC3, for which phase-shifted cycling describes dorsoventral bend propagation along the body axis (Fig. 4f; Fig. 4-Supp. 2c), reminiscent of sinuous crawling in larvae and adults. Thus, the posture library captures a developmental progression from immature (dorsoventral flipping) to mature (sinusoidal crawling) embryo behavior.

2.5 Synaptic signalling is required for mature motion, but not dorsoventral flipping

The behavior of late-stage embryos exhibits several potential signatures of neuronal control (increasingly directed movement, dorsal coiling bias, and sinuous crawling). To establish a role for synaptic signalling, we analyzed *unc-13(s69)* mutants which have a nearly complete block in synaptic vesicle fusion and (consequently) profound movement defects [56]. In late-stage embryos (750 mpf), *unc-13* mutant movement was strongly impaired, as indicated by shorter seam cell trajectories and smaller diffusion coefficients (Fig. 5a). Although their motion was severely restricted, *unc-13* mutants continued subtle movements in place, suggesting that spontaneous muscle contractions persist even when synaptic transmission is blocked. By contrast, at 530 mpf seam cell diffusion coefficients for *unc-13* mutants were indistinguishable from controls (Fig. 5b), implying that synaptic transmission is not required for the behavior of immature embryos. To further investigate the role of synaptic transmission in immature behavior, we analyzed flipping, which is the most salient behavior at this stage. For this analysis, flips were defined as transitions between dorsal and ventral coiling, i.e. from fully dorsally to fully ventrally bent postures and vice versa. At 530 mpf, control and *unc-13* mutants flipped 3 to 4 times per minute, with 75% of the transitions executed in 10 seconds (Fig. 5c). Flips can be considered translations along the PC1 axis (Fig. 4f, Fig. 4-Supp. 2a, b). We used mean PC2 and PC3 amplitudes during the transition to define 4 flip motifs: PC2-, PC2+, PC3-, and PC3+ (Fig. 5d). We found that trajectories through posture space were indistinguishable in control and *unc-13* mutants. For example, in both genotypes, ventral to dorsal flips usually started in the tail, with intermediate postures having a posterior dorsal bend (i.e., the PC2- motif; Fig. 5d). Fig. 5e summarizes the prevalence of each flip motif. Note that dorsal to ventral flips were also more likely to initiate in the tail (i.e., the PC2+ motif; Fig. 5e). By contrast, locomotion in larvae (and older embryos; Fig. 4-Supp. 2c) is dominated by bends propagating from head to tail, likely requiring neuronal coordination. These results suggest that motion in immature embryos is largely independent of UNC-13-mediated synaptic transmission, although an immature form of synaptic transmission (not requiring UNC-13) cannot be ruled out.

2.6 Slow wave twitch (SWT): A rhythmic behavior dependent on the nervous system

To accelerate mutant analysis, we turned to the brightfield assay (Fig 3). The profound motility defect observed in late-stage *unc-13* mutant embryos by seam cell tracking (Fig. 5a) was not immediately obvious in the brightfield assay (Fig 6a), most likely due to the strong contribution of spontaneous muscle contractions to pixel intensity changes. In search of a synaptic influence on movement, we analyzed embryo twitching in the frequency domain. Isolating the *unc-13* dependent signal from the wild-type scalogram revealed the 20-40 mHz SWT feature described above (Fig. 6b). To quantify SWT, we scanned the twitch profile of each embryo for the 15 minutes in which 20-40 mHz most dominated the power spectrum. The SWT power ratio refers to the proportion of the power spectrum accounted for by the 20-40 mHz frequency band. In wild-type animals, the SWT power ratio consistently peaked about an hour before hatching (Fig. 6c). As suggested by the scalograms, peak SWT power ratios were markedly diminished in *unc-13* mutants compared to wild-type (Fig. 6d). Thus, SWT represents a rhythmic embryonic behavior with a period of 25-50 seconds that requires synaptic transmission.

To identify neurons required for SWT, we analyzed mutants disrupting specific neurotransmitters (Fig. 6d, Fig. 6-Supp. 1). Peak SWT power ratios were unaffected by loss of the vesicular transporters for biogenic amines (*cat-1* VMAT), glutamate (*eat-4* VGLUT), or GABA (*unc-47* VGAT). By contrast, peak SWT power ratios were strongly diminished in mutants lacking the vesicular transporter for acetylcholine (*unc-17* VAChT; Fig. 6d), indicating that cholinergic transmission plays a prominent role in generating SWT behavior. Although motility was generally decreased in *unc-17* mutants (Fig.6-Supp. 1), changes in the magnitude of motion alone cannot explain changes in the relative power of the SWT frequency band. The SWT power ratio quantifies the temporal structure of motion. Body wall muscles express two classes of nicotinic acetylcholine receptors: homopentameric ACR-16 receptors and heteropentameric levamisole receptors containing UNC-29 subunits [56, 57]. Mutants lacking UNC-29 had significantly reduced peak power ratios in the SWT frequency band and this defect was rescued by a transgene expressing UNC-29 in muscles (Fig. 6d). By contrast, peak SWT power ratios were unaffected in *acr-16* mutants (Fig. 6d). Thus, SWT requires cholinergic signalling through UNC-29-containing receptors in muscles. Peak SWT power ratios were also strongly diminished in mutants lacking two pro-neuropeptide processing enzymes (*egl-3* PC2 and *egl-21* CPE; Fig. 6d), implicating neuropeptide signalling in SWT behavior.

2.7 RIS release of FLP-11 neuropeptides and GABA promote SWT quiescence

Peak SWT behavior coincides with a period of increased pausing, as detected by seam cell tracking (Fig 2e, g); consequently, we hypothesized that signal in the 20-40 mHz frequency band was a consequence of brief quiescent bouts. Two neurons (RIS and ALA) are known to promote behavioral quiescence in larvae and adults [58, 32, 59, 60]. Prompted by these results, we asked if SWT behavior is disrupted in mutants lacking RIS (*aptf-1* AP-2) or ALA (*ceh-17* PHOX2A) function [58, 61, 59]. Consistent with a role for RIS, we found that peak SWT power ratios were markedly reduced in *aptf-1* mutants but were unaffected in *ceh-17* mutants (Fig. 7a). RIS neurons elicit larval quiescence by secreting neuropeptides encoded by the *flp-11* gene [32]. We found that *flp-11* mutants exhibited a superficially normal pattern of embryo motion (i.e., early and late active phases with an intervening period of decreased mobility), suggesting that the overall developmental progression of embryonic behavior was unaffected (Fig. 7b, Fig. 7-Supp. 1). By contrast, SWT behavior was dramatically reduced in *flp-11* mutants, as indicated by the absence of the 20-40 mHz feature in scalograms (Fig. 7b) and by a significantly reduced peak SWT power ratio (Fig. 7a). These data suggest that late-stage movement is structured by periodic release of FLP-11 from RIS, which results in increased power in the 20-40 mHz frequency band.

To further describe SWT behavior, we analyzed embryo postures at the developmental stage corresponding to peak SWT behavior. We found that pauses occurred throughout posture space (Video 1), suggesting that SWT quiescent bouts are not associated with specific body postures.

To directly relate RIS activity to embryo behavior, we simultaneously monitored motion and activity of the RIS cell body with a genetically encoded calcium sensor, GCaMP6f [62], fused to a calcium insensitive fluorophore, mCherry. Tracking GCaMP/mCherry ratios in the RIS cell body in embryos aged at least 645 mpf (Fig. 8a, b), we observed RIS calcium transients at a rate within the SWT frequency band (24.8 +/- 1.6 mHz, mean +/- SEM; Fig. 8c). By contrast, ALA neuron calcium transients occurred far less frequently (1.9 +/- 0.3 mHz, mean +/- SEM). In mutants lacking FLP-11 neuropeptides, the rate and duration of RIS transients were unaltered (Fig. 8c, d), however, transient amplitudes were significantly increased (Fig. 8e). Larger calcium transient amplitudes in *flp-11* mutants suggests that FLP-11 may inhibit RIS activity in an autocrine manner. Behavioral quiescence was substantially reduced but not eliminated in *flp-11* mutants (Fig. 8c, d). Using the onset of calcium transients to align behavior and fluorophore intensities (GCaMP and mCherry), we found that the GCaMP signal (and not the mCherry signal) was negatively correlated with head speed (Fig. 8f), confirming that RIS activation was associated with behavioral slowing. This relationship persisted in *flp-11* mutants, however compared to wild-type, the behavioral slowdown was more transient

(Fig. 8f) and less likely to lead to a pause (Fig. 8g). The residual behavioral slowing found in *flp-11* mutants could be mediated by another RIS neurotransmitter, e.g., GABA. Consistent with this idea, compared to *flp-11* single mutants, the behavioral slowdown and quiescence associated with RIS calcium transients was diminished in *flp-11;unc-25* GAD double mutants, which are deficient for GABA synthesis (Fig.8-Supp. 1). These results suggest that a prominent feature of late-stage embryonic behavior is a rhythmic pattern of quiescence elicited by two RIS neurotransmitters, FLP-11 and GABA. GABA release was associated with transient behavioral slowing, whereas FLP-11 release was essential for sustained pausing.

2.8 Sensory response during SWT is dampened by FLP-11

Other forms of quiescence are associated with diminished responsiveness to arousing stimuli. To see if SWT shares this property, we analyzed the behavioral response to light. In adults and larvae, short-wavelength light has been shown to elicit arousal via endogenous photoreceptor LITE-1 [63, 64, 65]. Here, we monitored motion and activity of the RIS cell body following a UVB light pulse (285 nm). In these experiments, a 10 second irradiance was delivered during peak SWT (1h before hatching). Stimulus trials were retrospectively identified as those occurring when RIS was active (RIS_{on}) or inactive (RIS_{off}). UVB elicited behavioral arousal in embryos (Fig. 9a, b). Rapid and robust arousal was apparent in both RIS_{off} and RIS_{on} trials (Fig. 9a), confirming that SWT quiescence was reversible. The duration of UVB evoked behavioral arousal was increased in *flp-11* mutants compared to control embryos (Fig. 9a-d; compare the post-stim speed in panels Fig. 9b versus Fig. 9d). Together, these results suggest that FLP-11 dampens responses to UVB during the peak SWT period. Coincident with behavioral arousal, UVB irradiance evoked an acute inhibition of RIS activity (Fig. 9a-d), as previously shown with blue light in larvae [33]. Given the negative correlation between RIS activation and head speed (Fig. 8f), inhibition of RIS likely contributes to the behavioral arousal elicited by UVB. Both UVB evoked behavioral arousal and RIS inhibition were eliminated in mutants lacking the LITE-1 photoreceptor (Fig. 9e, f).

To further investigate the impact of SWT on sensory responses, we used the brightfield twitch assay to monitor behavioral responses to longer wavelength visible light. Similar to UVB, visible light evoked an arousal response that was prolonged in *flp-11* mutants (Fig. 9-Supp. 1). Thus, arousal responses to aversive light stimuli are exaggerated in mutants lacking SWT quiescence. Unlike UVB, arousal elicited by visible light was followed by motion slightly (albeit significantly) lower than baseline (Fig. 9-Supp. 1). This inhibited motion was lost in *flp-11* mutants and may represent a homeostatic response to the arousing stimulus. Collectively, these results suggest that SWT quiescence is reversible and that behavioral responses to arousing stimuli are dampened by FLP-11 during SWT.

3 Discussion

Here we describe a systematic analysis of behavioral maturation in *C. elegans* embryos. Our analysis leads to three primary conclusions. First, embryos follow a stereotyped behavioral trajectory: early flips between dorsal and ventral coiling (most often initiated in the tail) slowing into a period of reduced motility, followed by emergence of mature behaviors (including sinuous crawling, directed motion, and rhythmic quiescent bouts; Fig. 10). Second, synaptic transmission is required for late-stage movement, but not for early dorsoventral flipping nor the intervening period of reduced motility. Third, the rhythmic bouts of behavioral quiescence punctuating late-stage movement are elicited by rhythmic RIS activation and secretion of two RIS transmitters, FLP-11 and GABA. Below we discuss the significance of these findings.

3.1 Three phases of embryonic behavior

Our results suggest that embryos exhibit a stereotyped program for behavioral maturation in the final few hours before hatching, which comprises at least three phases (early flipping, an intermediate phase of reduced motility, and a late phase of mature motion). This general progression was apparent by both seam cell tracking and by brightfield motility assays. It is likely that further analysis of posture libraries will identify additional embryonic behaviors.

Following elongation, embryo behavior was initially dominated by flipping between all dorsal and all ventral body bends (Fig. 4-Supp. 2a, b). Flipping behavior was not disrupted in *unc-13* mutants, implying that it does not depend on synaptic transmission (Fig. 5c, d). Flipping could be mediated by intrinsic oscillatory activity in muscles or by a form of neuronal signaling that persists in the absence of UNC-13 (e.g., gap junctions or an unconventional form of synaptic vesicle exocytosis). Because flipping comprises alternating all dorsal and all ventral bends, there must be some mechanism to produce anti-correlated ventral and dorsal muscle contractions. It will be interesting to determine what drives immature flipping and whether this early behavior is required in some way for the subsequent emergence of mature behaviors.

Early flipping behavior is followed by a period of decreased motion. This slowdown is apparently not neuronally evoked, as it requires neither neuropeptide processing enzymes nor UNC-13 (Fig. 6a, Fig. 6-Supp. 1). Slowing does coincide with a shift in the forces defining body morphology, from a squeeze generated by contraction of circumferential actin bundles of the epidermal cytoskeleton to containment within a tough, yet flexible extracellular cuticle [66]. This structural transition could impact behavior; however, preliminary experiments (not shown) suggest that reduced motion is a consequence of decreased muscle activity rather than a structural constraint limiting motion. A shift from cytoskeletal to exoskeletal control of body shape is likely reiterated at each larval molt and could contribute to molt-associated lethargus quiescence [67]. The brightfield motility assay promises to be a useful screening tool to further investigate this phenomenon.

Following the inactive phase, late-stage embryos exhibit a mature pattern of motion. Mature motion comprises sinusoidal crawling, prolonged bouts of forward and reverse motion, and a rhythmic pattern of brief quiescent bouts. All of these features are grossly disrupted in *unc-13* mutants (Fig. 5a), implying that they are driven by synaptic circuits. Our prior study suggests that bouts of directed motion are mediated by the forward and reversal locomotion circuits that operate post-hatching [16].

3.2   SWT, a rhythmic embryonic quiescence

We identify SWT as a rhythmic form of behavioral quiescence occurring late in embryogenesis. Osmotic stress and reduced insulin signalling also cause behavioral quiescence around hatching, which is accompanied by developmental arrest [19]. Salt and insulin regulated quiescence and SWT quiescence occur at a similar stage of embryonic development and both require FLP-11, suggesting that these two forms of quiescence are mechanistically related. Other forms of *C. elegans* behavioral quiescence have been described during larval molts (lethargus) [67] and in response to nutrient excess (satiety) [68], cellular stress (e.g., heat shock) [69, 70], starvation [71, 33], and physical restraint [72]. These quiescent states, particularly lethargus, have been shown to exhibit sleep-like properties: reversibility, reduced sensitivity to external stimuli, homeostatic regulation, and a stereotyped posture [67, 73, 74, 75, 76, 77, 78]. Lethargus also shares deep molecular conservation with sleep in other systems, such as regulation by both PERIOD [79, 80, 81, 82, 83] and AP-2 transcription factors [84, 58, 85, 86].

Among the various quiescent states, SWT shares several properties with lethargus quiescence. First, both are promoted by RIS release of FLP-11 (Fig. 6) [32]. Second, lethargus quiescence coincides with molting (i.e., cuticle replacement) and SWT peaks about an hour after the onset of cuticle synthesis (Fig. 10). The timing of SWT relative to cuticle synthesis suggests that SWT may be similar to a late stage of lethargus. Consistent with this idea, quiescent bout durations in the second half of lethargus ($\approx$10 seconds) [74] are similar to those seen in SWT (Fig. 8d). Furthermore, the transcriptional profile around the time of SWT matches that of larval molting [87]. Finally, like lethargus and sleep, SWT quiescence can be reversed by an arousing light stimulus. Arousal is prolonged in *flp-11* mutants relative to controls (Fig. 9, Fig. 9-Supp. 1), suggesting that responses to external stimuli are diminished during SWT. Despite these similarities, it is likely that further analysis will reveal important differences between SWT and lethargus. For example, during lethargus, stimulated arousal is followed by enhanced quiescence [77]. This homeostatic response is a behavioral hallmark of sleep. We had conflicting results for homeostatic effects during SWT. Following arousal with visible light, we saw a small reduction in embryo motion below baseline (Fig. 9-Supp. 1), which could represent a homeostatic increase in quiescence. By contrast, we saw no evidence for homeostatic effects following the UVB stimulus (Fig. 9a, b). This discrepancy could reflect differences in the arousing stimulus or differences in how embryo motion was tracked in the two assays (RIS tracking versus brightfield twitch profiles). A weak homeostatic drive is also consistent with SWT being analogous to a late stage of lethargus, when homeostatic regulation is greatly diminished [77].

Is SWT quiescence required for some aspect of early brain development? Correlated spontaneous activity is essential for the refinement and maturation of developing neuronal circuitry in a variety of contexts [88]. For example, following initial myogenic movements, behavioral maturation of Drosophila is dependent on patterned spontaneous neuronal activity in embryos [89, 90, 91]. Could RIS be influencing network connectivity by broadly structuring neuronal activity? Embryonic quiescence may also be a mechanism to preserve energy stores. In this scenario, disrupting sleep could predispose embryos to metabolic stress. Indeed, transcriptional stress responses are associated with sleep disruption in worms, flies, and mice [92, 93, 94, 95, 96]. It will be interesting to see if prenatal metabolic stress alters early brain development.

In summary, despite the presence of many important neurodevelopmental benchmarks, behavior during the final hours of *C. elegans* embryogenesis is largely unexplored. The embryonic posture library described here will provide a resource to test new hypotheses about how (and when) embryonic circuits assemble. Semi-automated tracking with MHHT should accelerate expansion of this resource, with the discovery of new embryonic behaviors providing an entry point to study nascent neuronal circuitry. The potential for recording pan-neuronal activity in unanesthetized

embryos executing well-defined behaviors [16] as a stereotyped connectome emerges [22], uniquely positions *C. elegans* to investigate fundamental aspects of early brain development.

4 Methods

4.1 Key resource table

Reagent type (species) or resource	Designation	Source or reference	Identifiers	Additional information
Strain, strain background, (*C. elegans*)	*wIs51*	`https://cgc.umn.edu/`	KP10922	*wIs51* [SCMp::GFP + *unc-119*(+)]
Strain, strain background, (*C. elegans*)	*unc-13*(*s69*); *wIs51*	This paper	KP9135	Fig. 5
Strain, strain background, (*C. elegans*)	N2 Bristol	`https://cgc.umn.edu/`	N2	Wild-type reference
Strain, strain background, (*C. elegans*)	*unc-47*(*e307*)	`https://cgc.umn.edu/`	CB307	
Strain, strain background, (*C. elegans*)	*unc-17*(*e245*)	`https://cgc.umn.edu/`	CB933	
Strain, strain background, (*C. elegans*)	*acr-16*(*ok789*)	`https://cgc.umn.edu/`	RB918	
Strain, strain background, (*C. elegans*)	*unc-29*(*x29*)	[97]	KP7858	
Strain, strain background, (*C. elegans*)	*eat-4*(*ky5*)	`https://cgc.umn.edu/`	MT6308	
Strain, strain background, (*C. elegans*)	*cat-1*(*e1111*)	`https://cgc.umn.edu/`	CB1111	
Strain, strain background, (*C. elegans*)	*egl-3*(*n150*)	`https://cgc.umn.edu/`	MT150	
Strain, strain background, (*C. elegans*)	*egl-21*(*n476*)	`https://cgc.umn.edu/`	MT1071	
Strain, strain background, (*C. elegans*)	*ceh-17*(*np1*)	`https://cgc.umn.edu/`	IB16	
Strain, strain background, (*C. elegans*)	*aptf-1*(*gk794*)	`https://cgc.umn.edu/`	HBR227	
Strain, strain background, (*C. elegans*)	*aptf-1*(*tm3287*)	`https://cgc.umn.edu/`	HBR232	
Strain, strain background, (*C. elegans*)	*flp-11*(*tm2706*)	`https://cgc.umn.edu/`	HBR507	

Strain, strain background, (*C. elegans*)	*unc-29(x29); nuTi233*	This paper	KP9744	*nuTi233[pat-10* p::NLS-wCherry-NLS::SL2::UNC-29]
Strain, strain background, (*C. elegans*)	*nuTi580*	This paper	KP10749	*nuTi580[flp-11* p::GCaMP6f::mCherry]
Strain, strain background, (*C. elegans*)	*goeEx737*	https://cgc.umn.edu/	HBR2256	*goeEx737[flp-24* p::SL1::GCaMP3.35::SL2::mKate2 + *unc-119*(+)]
Strain, strain background, (*C. elegans*)	*flp-11(tm2706); nuTi580*	This paper	KP10763	Fig. 8
Strain, strain background, (*C. elegans*)	*unc-25(e156); nuTi580*	This paper	KP10964	Fig. 8-Supp. 1
Strain, strain background, (*C. elegans*)	*unc-25(e156); flp-11(tm2706); nuTi580*	This paper	KP10965	Fig. 8-Supp. 1
Strain, strain background, (*C. elegans*)	*lite-1(ce314); nuTi580*	This paper	KP10762	Fig. 9
Strain, strain background, (*E. coli*)	OP50	[98]	OP50	Worm food
Recombinant DNA reagent	*pat-10* p::NLS-wCherry-NLS::SL2::UNC-29	This paper	KP#4524	UNC-29 expression in muscle
Recombinant DNA reagent	*flp-11* p::GCaMP6f::mCherry	This paper	KP#4525	GCaMP expression in RIS
Chemical compound, drug	poly-L-lysine	Sigma-Aldrich	P2636	
Software, algorithm	MATLAB	MathWorks	MATLAB R2018a	
Software, algorithm	MHHT	This paper		https://github.com/lauziere/MHHT
Other	UVB LED	Marktech Optoelectronics	MTSM285	Fig. 9

4.2 Strains and reagents

Animals were maintained on nematode growth medium (NGM) seeded with *Escherichia coli* (OP50) as described in [98]. The posture library was built using *wIs51[SCM*p::GFP + *unc-119*(+)], which expresses GFP in hypodermal seam cell nuclei. For the supplemental postures described in Fig. 4-Supp. 1, *wIs51* was combined with epidermal actin marker, *mcIS50[lin-26*p::vab-10(actin-binding domain)::GFP + *myo-2*p::GFP] and one of the following mCherry transgenes: *stIs10131[elt-7*p::H1-wCherry + *unc-119*(+)] (SLS20), *stIs10501[ceh-36*p::H1-wCherry::his-24p::mCherry + *unc-119*(+)] (SLS21), *stIs10691[ref-1*p::H1-wCherry + *unc-119*(+)] (SLS22), *nuSi187[pat-10*p::NLS-GCaMP::mCherry-NLS] (SLS23), *stIs10138[tbx-38*p:: H1-wCherry; *unc-119*(+)] (SLS24), or *stIs10808[nob-1*p::H1-wCherry; *unc-119*(+)] (SLS25).

For rescuing *unc-29* expression in muscle, plasmid KP#4524 was generated by inserting the *pat-10* promoter (550 bp), the SV40 nuclear localization sequence, mCherry with introns, the EGL-13 nuclear localization sequence, the *gpd-2* 3' UTR with SL2 acceptor site, *unc-29* cDNA, and the *unc-54* 3' UTR between the SpeI and AgeI sites in pCFJ910.

10

For calcium imaging in RIS, plasmid KP#4525 was generated by inserting the *flp-11* promoter (3159 bp), GCaMP6f with introns, a flexible linker (GSSTSG(AP)$_7$ASEF), mCherry with introns, and the *unc-54* 3' UTR between the SbfI and StuI sites in pCFJ910.

The miniMOS method [99] was used to integrate KP#4524 and KP#4525, generating single copy insertions: *nuTi233*[*pat-10*p::NLS::mCherry::SL2::UNC-29] and *nuTi580*[*flp-11*p::GCaMP6f::mCherry].

Recordings were acquired at room temperature. Embryonic age was determined by measuring the time elapsed since twitch onset (defined as 430 mpf).

4.3 Posture library

4.3.1 Sample preparation

Gravid adults were dissected to release embryos, which were transferred to a patch of poly-L-lysine (1 mg/mL) in a diSPIM imaging chamber filled with M9 buffer. Embryo orientation was set to minimize Z-steps, i.e., objective translation along the embryo's minor axis. Prior to fluorescence imaging, brightfield recordings were acquired to stage the embryos.

4.3.2 Microscope

On a diSPIM [40], a pair of perpendicular water-dipping, long-working distance objectives (40x, 0.8 NA) were used for brightfield and fluorescence imaging. Acquisition was controlled using Micro-Manager's diSPIM plugin (`https://micro-manager.org/`). Note that although the diSPIM can collect two orthogonal views, only a single view was used to build posture libraries, i.e., iSPIM mode. Sweeping a 488 *nm* laser beam (measured $<1\ \mu W$ after the objective), a two-dimensional MEMS mirror in the diSPIM scanhead generated the light-sheet and defined the image volume. To maximize speed, the camera (pco.edge 4.2 or ORCA-Flash 4.0) was oriented such that the chip readout direction was along the embryo's minor axis. The imaging objective was translated in step with the light-sheet, generating 36 planes at inter-plane spacing of 1.2 μm. Exposure time per plane was 4 milliseconds and volumes were acquired at 3 Hz. To reduce file size, the camera was set to 4x binning, resulting in 16-bit images with 0.65 μm pixels. See [100] for detailed protocols on imaging embryos with the diSPIM.

For the supplemental postures described in Fig. 4-Supp. 1, diSPIM acquisition parameters were optimized for spatial resolution rather than speed. Specifically, diSPIM mode was used to acquire image volumes from perpendicular objectives with no pixel binning at the camera. The two orthogonal views were then computationally fused to generate isotopically resolved image volumes [39, 101]. Laser power was at least an order of magnitude greater than for the volumes acquired at 3 Hz (i.e., $> 30\ \mu W$, measured after the objective). The 561 *nm* laser line was scanned simultaneously, with dual-color image splitters separating detection at the camera (W-VIEW GEMINI, Hamamatsu). Volumes were acquired every 5 minutes from pre-twitching until hatching, with each image volume comprising 50 planes at a spacing of 1 μm. Exposure time per plane was 5 milliseconds, with volumes acquired in <900 milliseconds.

4.3.3 Analysis

Image volumes were segmented using a large kernel 3D U-Net trained on an average of the Dice coefficient and binary cross-entropy loss functions. See below for additional details on image segmentation. In a volume with good detections, seam cells were manually positioned along the body axis by observing movement over several frames. From this seed volume, cell positions were tracked across time using MHHT. See below for additional details on MHHT.

Left and right seam cells were fit with natural cubic splines using MATLAB's "cscvn" function. DV bends were then computed from the midpoint (mL/R) along the spline connecting adjacent seam cells and the corresponding midpoint (mR/L) on the opposite side of the body (Fig. 4a). For example, for the DV bend between H0L and H1L:

- $\vec{v}_1$ connects mL to H0L;

- $\vec{v}_2$ connects mR to mL;

- $\vec{v}_3$ connects mL to H1L; and

- DV bend $= arctan2(([\vec{v}_1 \times \vec{v}_2] \times [\vec{v}_2 \times \vec{v}_3]) \cdot \frac{\vec{v}_2}{|\vec{v}_2|}), [\vec{v}_1 \times \vec{v}_2] \cdot [\vec{v}_2 \times \vec{v}_3])$

The MATLAB class "msdanalyzer" was used to evaluate mean square displacement [102].

4.4 Brightfield motion assay

4.4.1 Sample preparation

Several ($\geq$ 4) gravid adults per strain were dissected directly in an M9 filled glass bottom microwell imaging dish (MatTek Corp., P35G-1.5-20-C). Up to 60 pre-twitching embryos were arrayed on a patch of poly-L-lysine (0.1 mg/mL) using water currents generated with a worm pick. Worm remains and unwanted embryos were removed with a micropipette and the dish was lidded.

4.4.2 Microscope

Embryo arrays were recorded on an inverted microscope (Zeiss, Axiovert 100) with a 5x, 0.25 NA objective. A CCD camera (CoolSNAP HQ2) generated 16-bit images with a pixel size of 1.29 μm Transmitted light power was adjusted to get background pixel counts of $\approx$500 from a 2 millisecond exposure. Images were acquired at 1 Hz using Micro-Manager control software.

4.4.3 Analysis

Pixel intensities were extracted from a box (21x21 pixels) centered on each embryo and frame to frame pixel intensity changes larger than threshold (25) were tallied. The onset of sustained twitching was detected as the first tally (smoothed over 30 frames) greater than 120 of a potential 441 pixels. Background intensity for each frame was also extracted from a perimeter around the embryo (61x61 pixels). Hatching was detected as the point at which the mean intensity at the embryo position (smoothed over 30 frames) approximated the mean intensity of the background perimeter (signal-to-background ratio of at least 0.92). Fresh hatchlings occasionally swam into the field of view, registering pixel changes in the embryo and background. Data were therefore excluded for frames in which the background registered changes greater than threshold (35) in more than X pixels (40 of a potential 240 when smoothed over 30 frames).

Peak SWT power ratios were computed as follows:

1. For each embryo, 15 min twitch profiles were extracted with a sliding window (200 second step size) from 1 hour post twitch until hatching. Missing datapoints were replaced with a reversed duplication of the immediately preceding interval of the same length.

2. Using MATLAB's Fast Fourier transform ("fft") function, each 15 minute twitch profile was transformed from the time domain (i.e., pixels changing per second, $y(t)$) to the frequency domain, $Y(f)$ for equally spaced frequency bins from $f_0 = 0$ to $f_{900} = 1$ Hz, i.e., the sampling rate.

3. For each 15 minute twitch profile, the proportion of the signal attributed to the SWT frequency band was computed:

$$\text{SWT power ratio} = \frac{\sum_{20 \text{ mHz} \leq f \leq 40 \text{ mHz}} |Y(f)|^2}{\sum_{0 \leq f \leq 500 \text{ mHz}} |Y(f)|^2}$$

4. For each embryo, the timing and magnitude of the largest SWT power ratio was recorded.

To estimate a baseline for peak SWT power ratios (i.e., the dashed lines in Figs. 6d, 7a), pairs of neighbouring values were randomly shuffled prior to the discrete Fourier transformation (between steps 1 and 2 above) for a sample of wild-type embryos.

Scalograms were generated using MATLAB's Continuous 1-D wavelet transform ("cwt") function (with "morse" wavelet).

Each genotype was evaluated in at least two independent experiments. Because coordinated aspects of motion are not discerned, all movements detected by the brightfield assay are referred to as twitches, regardless of the age of the embryo. The "slow wave" terminology refers to the relatively low frequency band (20-40 mHz) for which SWT is defined.

4.5 Calcium Imaging

4.5.1 Sample preparation

Several ($>=$15) gravid adults per strain were dissected directly in an M9 filled glass bottom microwell imaging dish (MatTek Corp., P35G-1.5-20-C). Embryos with no more than 4-cells were selected using currents generated with a

worm pick and stuck to a patch of poly-L-lysine (0.1 mg/mL) in pairs, aligned end to end along their major axis (a configuration that enabled imaging two embryos per scan). Worm remains and unwanted embryos were removed with a micropipette and the dish was lidded. Prior to calcium imaging, the brightfield assay (see above) was used to time first twitch.

4.5.2 Microscope

At least 215 minutes after the onset of twitching (i.e., $\approx$645 mpf), embryos were imaged on an inverted confocal microscope (Nikon, Eclipse Ti2) using a 20x, 0.75 NA objective. Resonant scanning in two directions generated image planes of 1024x256 pixels (0.16 μm/pixel) for two channels (488 and 561 nm lasers) in 33.3 milliseconds. Two embryos were imaged per scan. Volumes were acquired at 1 Hz for 5 minutes using a piezo stage stepping 7.875 μm between 5 image planes (note that the pinhole was opened to minimize the number of steps required to span the embryos).

4.5.3 Analysis

RIS cell body position and corresponding GCaMP and mCherry intensities were extracted from an image volume cropped around a single embryo. Specifically, following background subtraction (pixel counts-100), each image plane was filtered using a Gaussian smoothing kernel with standard deviation of 5 (MATLAB's "imgaussfilt" function with "symmetric" image padding to prevent edge artifacts). The position of the RIS cell body was identified in the mCherry channel as the brightest pixel of the filtered volume. The corresponding intensity in the filtered GCaMP channel was used to compute $\Delta R/R_0 = (R - R_0)/R_0$, where R is the GCaMP/mCherry ratio and R_o is the ratio at baseline, set as the 10th percentile for each trace. Calcium transients were identified in smoothed traces (moving mean with span 4) using an onset threshold of $\Delta R/R_0 \geq 2$ and an offset threshold of $\Delta R/R_0 < 1.5$. For ALA, only a single calcium transient was detected at the cell body in 5 min recordings from 42 embryos. However, calcium transients in ALA neurites were detectable using the mean pixel count of maximum intensity projections (onset threshold: $\Delta R/R_0 \geq 0.07$ and offset threshold: $\Delta R/R_0 < 0.05$.

4.6 Seam Cell Nuclei Detection

Traditional methods for blob detection such as Watershed [103] and Laplacian of Gaussians (LoG) [43, 44] were compared to a variety of deep learning based approaches [104, 42, 105](Table 2). Each detection method yields a set of detected objects per image volume. A linear program was used to match detections to annotations at each frame of the annotation set. One-to-one matching aligned annotated nuclei centers and detection cluster centers per volume across the test set. The average precision, recall, and F1 score across test set volumes are reported in Table 2.

Given its superior performance, a 3D U-Net style convolutional neural network (CNN) was employed to perform semantic segmentation on the *C. elegans* embryo image volumes [41, 42]. The established 3D U-Net was augmented to use a size $(5, 5, 5)$ kernel, as opposed to the original $(3, 3, 3)$ kernel, extending the field of view at each layer. Strided 3D convolution layers downsample by a factor of two across lateral dimensions while preserving axial resolution. The limited axial resolution encodes more information per planar image due to the explicit downsampling occurring during imaging. The number of filters in each layer doubles from 16 to 32, 64, 128 when downsampling. The loss function is the sum of the binary cross-entropy and negative dice coefficient losses. The cross-entropy portion prioritizes accurate prediction of challenging individual voxels between close nuclei, but may produce noisy predictions. In juxtaposition, the dice coefficient prioritizes structural similarity in clusters of voxels constituting nuclei, but is known to consolidate sigmoid outputs at extreme values 0 and 1, limiting the model's ability to smoothly identify uncertainty in voxel prediction [106]. Denote $\mathbf{y} \in \{0,1\}^{X \times Y \times Z}$ and $\hat{\mathbf{y}} \in [0,1]^{X \times Y \times Z}$ as the binary ground truth and sigmoid output tensors respectively. The loss can then be written:

$$\mathcal{L}(\mathbf{y}, \hat{\mathbf{y}}) = \underbrace{- \sum_{i=1}^{X} \sum_{j=1}^{Y} \sum_{k=1}^{Z} [y_{ijk} \log(\hat{y}_{ijk}) + (1 - y_{ijk})(\log(1 - \hat{y}_{ijk})]}_{\text{Cross Entropy}} + \underbrace{\frac{-2 \sum_{i=1}^{X} \sum_{j=1}^{Y} \sum_{k=1}^{Z} y_{ijk} \hat{y}_{ijk}}{\sum_{i=1}^{X} \sum_{j=1}^{Y} \sum_{k=1}^{Z} (y_{ijk}^2 + \hat{y}_{ijk}^2)}}_{\text{Dice Coefficient}}$$

The model was trained via the Adam optimizer with an initial learning rate of $7.5 * 10^{-5}$ [107]. The model yields image volumes of the same size as the input microscope image volumes, containing values $y_{ijk} \in [0, 1]$. Each volumetric output is thresholded conservatively (output voxels $y_{ijk} \geq 0.95$ are predicted to be part of a seam cell nucleus) in order to minimize incorrectly predicted voxels between apparently close nuclei, while simultaneously ensuring dim nuclei are captured by at least a few correctly predicted voxels. Supervoxels defined as disjoint clusters of the binarized

output volume are returned as predicted instances of seam cell nuclei. The centroids of detected supervoxels serve as the detection set for each image volume.

4.7 Multiple Hypothesis Hypergraph Tracking

Each imaged embryo yields a sequence of ≈54000 image volumes which are processed in batch by our large kernel 3D U-Net. The CNN with post-processing produces detected objects in each image volume. The initial set of detections may contain nuclei clumped together and misclassified as a single detection, spurious voxels (false positives), or may miss dim nuclei (false negatives). Seam cell nuclei tracking is cast as a traditional multiple object tracking (MOT) problem; all seam cell nuclei positions together are referred to as the posture at each frame.

Multiple Hypothesis Tracking (MHT) [47, 48, 49] is the foremost paradigm for MOT, especially when tracking objects imaged with fluorescence microscopy [108, 109]. MHT tracks objects independently by using linear motion models to describe object trajectories in a "deferred decision" logic, leveraging smooth motion over several future frames to disentangle competing tracks. However, the sporadic twitches and rapid changes in frame-to-frame behavior preclude predictive modeling of seam cell nuclei locations. Also, MHT is unable to model relationships between objects in deciding track updates. The interdependence of seam cell nuclei movement inspired our proposed paradigm for flexibly integrating correlated object motion into MOT applications.

Multiple Hypothesis Hypergraph Tracking (MHHT) was developed as an extension of MHT to more effectively maintain an accurate representation of the *C. elegans* posture throughout late-stage embryogenesis by leveraging correlated seam cell motion. Relationships between seam cell nuclei were used to give enhanced context at the data association step, in which each detection is identified as a unique seam cell nucleus or designated debris. MHHT uses hypergraphs to characterize relationships between seam cells. Hypergraphs enable richer characterizations of object relationships than is possible with graphical approaches. Our best hypergraphical model considers simultaneous assignments of many detections to nuclear identities to rank posture hypotheses. This model is then fit using seam cell nuclei coordinates from a second imaged embryo to weight hypergraphical features, further informing the quantification of frame-to-frame movements.

MHHT adapts hypothesis oriented MHT [47, 49] to include graphical interpolation for missed detections and hypergraphical evaluation of sampled hypotheses. In summary, Murty's algorithm identifies the K best solutions to the standard linear data association problem [110, 111]. This association problem, known as the gated Global Nearest Neighbor (GNN) approach, treats objects as independent, with motion confined to a limited region, referred to as a gate. The gate specifies which detections can be associated to each track; i.e, seam cell nuclei gates which contain no detections are reported missing, and will be graphically interpolated. Furthermore, a hypergraphical association function f measures the cost of the complete posture update: $\mathbf{Z}^{(t)}$. This process is iterated recursively across N future frames to contextualize the state update at time t. The exploration forms an exponentially growing search tree in which paths from the initial state $\mathbf{Z}^{(t-1)}$ expand into K solutions. Each of the K solutions following interpolation yields a hypothesized state $\mathbf{Z}(\hat{t}, k)$, initiating a recursion, adding to the cost of association at frame t. The states $\mathbf{Z}(\hat{t}, k)$ of the path with minimum summed hypergraphical association cost is chosen at frame t.

Anatomical constraints allow for physical models to contextualize embryonic movement. The models themselves are expressed as graphs or hypergraphs. Fig. 1c depicts a graphical representation of an embryo used as a basis for modeling posture track updates. Edges appear along sides posterior to anterior, laterally between pairs of nuclei, and diagonally between sequential pairs. The first graphical association model, denoted *Embryo*, compares changes in edge lengths frame-to-frame to comprise the cost of the track update. Annotated data are used to estimate statistics of a parametric model to further describe embryonic behavior. Two such models, *Posture* and *Movement*, are explored to track posture. *Posture* is the data-driven enhancement of *Embryo*; the hypergraphical model measures the consistency in the shape of the embryo throughout successive frames. *Movement* is then a data enhanced version of the GNN filter, a graphical model evaluating patterned movement between nuclei.

The embryo graph $G = (V, E)$ specifies a set of edges E connecting seam cells locally. The attributed graph arising from established tracks $\mathbf{g}^{(t-1)} := \mathbf{g}(\mathbf{Z}^{(t-1)}; E)$ contextualizes the state $\mathbf{Z}^{(t-1)}$, serving as a basis for comparison across hypotheses at time t. Hypotheses evaluated at time t: $\hat{\mathbf{g}}^{(t)} := \mathbf{g}(\hat{\mathbf{Z}}^{(t)}; E)$ describe the posture of the embryo according to predicted states at time t. Frame-to-frame differences in the attributed representations are assumed multivariate Gaussian: $(\hat{\mathbf{g}}^{(t)} - \mathbf{g}^{(t-1)}) \sim \mathcal{N}(\mathbf{0}, \mathbf{\Sigma})$. The Mahalanobis distance f is used to evaluate a hypothesized state representation:

$$f(\hat{\mathbf{g}}^{(t)}, \mathbf{g}^{(t-1)}; \hat{\mathbf{\Sigma}}^{-1}) = \sqrt{(\hat{\mathbf{g}}^{(t)} - \mathbf{g}^{(t-1)})' \hat{\mathbf{\Sigma}}^{-1} (\hat{\mathbf{g}}^{(t)} - \mathbf{g}^{(t-1)})}$$

The covariance matrix Σ is estimated from a corpus of annotated data. States of all n objects from frames $t = 1, 2, \ldots, T$ are used as pairs $\{(\mathbf{Z}^{(1)}, \mathbf{Z}^{(2)}), (\mathbf{Z}^{(2)}, \mathbf{Z}^{(3)}), \ldots, (\mathbf{Z}^{(T-1)}, \mathbf{Z}^{(T)})\}$ to estimate frame-to-frame variation in pairs of hyperedge differences: $\{(\mathbf{g}^{(1)}, \mathbf{g}^{(2)}), (\mathbf{g}^{(2)}, \mathbf{g}^{(3)}), \ldots, (\mathbf{g}^{(T-1)}, \mathbf{g}^{(T)})\}$. Define $\bar{\mathbf{g}} = \frac{\sum_{t=1}^{T} \mathbf{g}^{(t+1)} - \mathbf{g}^{(t)}}{T-1}$. Then, the covariance matrix is estimated:

$$\hat{\boldsymbol{\Sigma}} := \frac{1}{T-1} \sum_{t=1}^{T} (\mathbf{g}^{(t+1)} - \mathbf{g}^{(t)} - \bar{\mathbf{g}})(\mathbf{g}^{(t+1)} - \mathbf{g}^{(t)} - \bar{\mathbf{g}})'$$

The *Embryo* and *Posture* models penalize associations which distort the embryo's shape. The bottom graph of Fig. 1c highlights correlated changes in edge length relative to the V2L-V3L edge. Edges between track states vary in length as the embryo moves frame to frame. Denote the edges $E = [e_1, e_2, \ldots, e_M]$, where edge $e_j = (u_j, v_j)$ describes a relationship between nuclei u_j and v_j. Each vector $\mathbf{e}_j^{(t)} = \mathbf{z}_{u_j}^{(t)} - \mathbf{z}_{v_j}^{(t)}$ describes the chord connecting states of nuclei u_j and v_j at time t. Then, the vector $\mathbf{E}^{(t)} = [\|\mathbf{e}_1^{(t)}\|_2, \|\mathbf{e}_2^{(t)}\|_2, \ldots, \|\mathbf{e}_M^{(t)}\|_2]$ describes lengths of these chords. Differences in chord lengths between frames $\mathbf{E}^{(t)}$ - $\mathbf{E}^{(t-1)} \in R^{M \times 1}$ form the basis of the association cost. Then, the *Embryo* model is defined:

$$f_E(\hat{\mathbf{Z}}^{(t)}, \mathbf{Z}^{(t-1)}) = \sqrt{(\hat{\mathbf{E}}^{(t)} - \mathbf{E}^{(t-1)})'\mathbf{I}(\hat{\mathbf{E}}^{(t)} - \mathbf{E}^{(t-1)})} = \sum_{j=1}^{M} \sqrt{(\hat{\mathbf{E}}^{(t)} - \mathbf{E}^{(t-1)})^2} \tag{1}$$

Annotated data are used to estimate covariances between the M differences across state updates. The resulting covariance matrix $\hat{\Sigma}_P$ scales differences in chord lengths among the M chords present in G to yield the *Posture* model:

$$f_P(\hat{\mathbf{Z}}^{(t)}, \mathbf{Z}^{(t-1)}; \hat{\boldsymbol{\Sigma}}_P^{-1}) = \sqrt{(\hat{\mathbf{E}}^{(t)} - \mathbf{E}^{(t-1)})'\hat{\boldsymbol{\Sigma}}_P^{-1}(\hat{\mathbf{E}}^{(t)} - \mathbf{E}^{(t-1)})} \tag{2}$$

Both *Embryo* and *Posture* are further characterized by the unary costs given by the gated GNN and the evaluated hypothesis $\varphi^{(t)}$: $\sum_{i=1}^{n} \mathbf{C}_{i, \varphi^{(t)}}$.

Movement extends the traditional GNN cost to penalize *unnatural* movement between states. The distance between states at $t-1$ and t, $\sum_{i=1}^{n} \|\mathbf{z}_i^{(t)} - \mathbf{z}_i^{(t-1)}\|_2$, can be scaled by the inverse covariance matrix describing motion between pairs of nuclei. The states $\mathbf{z}_i^{(t)} = [x_i^{(t)}, y_i^{(t)}, z_i^{(t)}]$ and $\mathbf{z}_j^{(t-1)} = [x_j^{(t-1)}, y_j^{(t-1)}, z_j^{(t-1)}]$ can be expressed as element-wise differences:

$$\mathbf{Z}^{(t)} - \mathbf{Z}^{(t-1)} = \begin{bmatrix} \mathbf{z}_1^{(t)} \\ \mathbf{z}_1^{(t)} \\ \mathbf{z}_1^{(t)} \\ \vdots \\ \mathbf{z}_n^{(t)} \end{bmatrix} - \begin{bmatrix} \mathbf{z}_1^{(t-1)} \\ \mathbf{z}_2^{(t-1)} \\ \vdots \\ \mathbf{z}_n^{(t-1)} \end{bmatrix} = \begin{bmatrix} x_1^{(t)} \\ y_1^{(t)} \\ z_1^{(t)} \\ x_2^{(t)} \\ y_2^{(t)} \\ z_2^{(t)} \\ \vdots \\ x_n^{(t)} \\ y_n^{(t)} \\ z_n^{(t)} \end{bmatrix} - \begin{bmatrix} x_1^{(t-1)} \\ y_1^{(t-1)} \\ z_1^{(t-1)} \\ x_2^{(t-1)} \\ y_2^{(t-1)} \\ z_2^{(t-1)} \\ \vdots \\ x_n^{(t-1)} \\ y_n^{(t-1)} \\ z_n^{(t-1)} \end{bmatrix} = \begin{bmatrix} x_1^{(t)} - x_1^{(t-1)} \\ y_1^{(t)} - y_1^{(t-1)} \\ z_1^{(t)} - z_1^{(t-1)} \\ x_2^{(t)} - x_2^{(t-1)} \\ y_2^{(t)} - y_2^{(t-1)} \\ z_2^{(t)} - z_2^{(t-1)} \\ \vdots \\ x_n^{(t)} - x_n^{(t-1)} \\ y_n^{(t)} - y_n^{(t-1)} \\ z_n^{(t)} - z_n^{(t-1)} \end{bmatrix} \in R^{3n \times 1} \tag{3}$$

Each pair of nuclei has an estimable 3×3 covariance matrix specifying the relationship between movement along each axis. The resulting block $3n \times 3n$ covariance matrix, $\boldsymbol{\Sigma}_M$ then scales the difference between states:

$$f_M(\hat{\mathbf{Z}}^{(t)}, \mathbf{Z}^{(t-1)}; \hat{\boldsymbol{\Sigma}}_M^{-1}) = \sqrt{(\hat{\mathbf{Z}}^{(t)} - \mathbf{Z}^{(t-1)})'\hat{\boldsymbol{\Sigma}}_M^{-1}(\hat{\mathbf{Z}}^{(t)} - \mathbf{Z}^{(t-1)})} \tag{4}$$

The *Posture* and *Movement* models are combined additively to produce the *Posture-Movement* (*PM*) model. Readers are referred to https://github.com/lauziere/MHHT and [50] for further details on MHHT methodology.

5   Acknowledgements

Model	Precision	Recall	F1	Citation	Implementation
IFT-Watershed	0.81	0.80	0.80	[103]	[112]
LoG-GSF	0.95	0.90	0.92	[43, 44]	[45]
Wavelet	0.88	0.86	0.87	[113]	[114]
Mask-RCNN	0.93	0.89	0.91	[104]	[115]
3D U-Net Dice	0.94	0.91	0.92	[42]	[116]
3D U-Net Dice/BCE	0.95	0.92	0.93	[42]	[116]
Stardist 3D	0.91	0.88	0.89	[105]	[117]

Table 2: **Seam cell nuclei detection results on a held out test set.** The variance in apparent size, shape, proximity, and intensity patterns make seam cell nuclei detection challenging. A held-out test set of image volumes was annotated by an expert; centers of seam cell nuclei were used as reference to compare automatic detection methods. A variety of methods were compared, with recent deep learning based methods yielding the most accurate detections, on average (across 46 held-out test image volumes). The large kernel 3D U-Net trained on both the dice coefficient (Dice) and binary cross-entropy (BCE) yields both the highest precision and recall. However, even the 3D U-Net cannot reliably detect all seam cell nuclei in an image volume.

Figure 1: **Tracking seams cells with Multiple Hypothesis Hypergraph Tracking (MHHT).** a) A timeline of embryo development is shown with the imaging window highlighted. mpf: minutes post fertilization. b) The scheme utilized for seam cell identification is shown. Left: A representative image of hypodermal seam cell nuclei (XY maximum intensity projection). Scale bar, 10 μm. Middle: Output of the 3D U-Net segmentation. Right: Seam cell identifications made by MHHT. See Fig. 1-Video 1. c) To illustrate the interdependence of seam cell movement, correlation in X-axis (labelled in b) motion of the V2 seam cell with all other seam cells is shown (top). To illustrate local constraints on the distance between neighboring seam cells, correlation of V2-V3 distance with indicated edge lengths is shown (bottom). See Fig. 1-Supp. 1 for full correlation matrices. d) A posture assignment search tree with width K=2 and depth N=3. Physically impossible body contortions (self-intersections) are pruned (scissors). The path accruing the least cost is highlighted (outlined circles).

Figure 1 - Figure Supplement 1: Correlation matrix for seam cell displacement along the X-axis of the image (Fig. 1b). b) Correlation matrix for changes in edge length.

Figure 1 - Video 1: An embryo at 540 mpf expressing GFP in hypodermal seam cell nuclei. XY maximum intensity projection (left) with segmented (center) and identified seam cell nuclei (right). Original data acquired at 3 Hz.

Figure 2: **Transition to punctuated and directed movement ahead of hatching.** a) Mean square displacement (MSD) for each seam cell nucleus is plotted. Dotted line indicates predicted unconfined Brownian motion for the H1 seam cell. b) Mean diffusion coefficient (D) over the entire recording is plotted for each seam cell pair. X-axis label colored as in a). Individual embryo values (grey) and mean +/- SEM (black) are shown. c) Diffusion coefficients for all seam cells were computed over 20 minute bins. Individual embryo values (grey) and mean +/- SEM (black) are shown. d) 20 minute trajectories are shown for the H1 and V6 seam cell at the indicated ages (left). Cell velocity ('v') is indicated by the shade of tracks (see velocity LUT). Direction of motion along the anteroposterior axis ('θ') is indicated by pink and blue. A schematic illustrating how 'v' and 'θ' are defined is shown (right). e) Embryo speed is plotted from 530-808 mpf. Forward, reverse, and pausing bouts are highlighted in 5 minute embryo speed traces (bottom). Forward and backward movement were defined as θ less than 45$_o$ and greater than 135º, respectively. Pauses were defined as speed $< 0.5 \mu m$/s. f) Coefficient of variation in embryo speeds for 20 minute bins are plotted. Individual embryo values (grey) and mean +/- SEM (black) are shown. g) Mean duration of forward, backward, and pausing bouts in 20 min bins are plotted. Individual embryo values (faint traces) and mean +/- SEM (bold traces) are shown.

Figure 3: **A brightfield motility assay reveals a stereotyped pattern of embryonic behavior maturation.** To independently assess embryo behavior, we developed a brightfield motility assay. Motion of each embryo is estimated by the fraction of pixels changing intensity between frames. The "twitch profiles" only report crude motion and are unable to distinguish more detailed aspects of behavior (e.g., direction or posture). a) Embryos arrayed for a brightfield assay are shown (left). Scale bar, 100 μm. Higher magnification views of the highlighted embryo (scale bar, $10 \mu m$ over 3 consecutive frames and frame subtraction images are shown (right). A representative twitch trace illustrating proportion of pixels changing at twitch onset ($\approx$430 mpf) is shown (bottom). Fig. 3-Video 1 shows a representative brightfield recording. b) Top: Average pixel changes aligned at twitch onset are plotted (in 20 minute bins). Individual embryo values (grey) and mean +/- SEM (black) are shown for n=40 embryos. Bottom: Brightfield twitch profile, with each line corresponding to a single embryo. Proportion of pixels changing intensity (smoothed over 10 seconds) is indicated by the color LUT. c) Coefficient of variation of pixel changes aligned at twitch onset (in 20 minute bins) are plotted. Individual embryo values (grey) and mean +/- SEM (black) are shown. d) Mean twitching scalogram is shown. The signal in the 20-40 mHz frequency band around 670 to 710 mpf (arrow) represents the SWT behavior.

Figure 3 - Supplement 1: a) Time from twitch to SWT versus twitch to hatch for 31 brightfield recordings of wild-type embryos. Sorted by time to hatch. SWT identified as peak relative power in the 20-40 mHz frequency band. Each dot represents an embryo, with mean +/- SEM.

Figure 3 - Video 1: An embryo array for the brightfield assay. Original data acquired at 1 Hz.

Figure 4: **Eigen-embryos compactly describe behavioral maturation.** a) A schematic illustrating how dorsoventral (DV) bends are defined. Top: Seam cell nuclei on each side of the body are fit with a natural cubic spline (black line). Vector $\bar{v}_2$ links the midpoints between adjacent seam cell nuclei (open circles). Bottom: View looking down $\bar{v}_2$2 to highlight a DV bend angle on one side of the body (red arrow). b) DV bend angles between all adjacent seam cells are used to define an embryo's posture. DV bends along the left (+) and right (o) sides of an embryo (top) are plotted (top). The posture model for this embryo is shown (bottom). Position along the anteroposterior axis is indicated by the color gradient. c) The fraction of the total variance captured by reconstructing postures using 1 through all 18 principal components is plotted. d) Fraction of the total variance captured by the first 4 principal components is plotted as a function of embryo age (mpf). e) Eigen-embryos (i.e., eigenvectors for the first 4 PCs) derived from the 3 individual embryos in grey and from pooled datasets in color (left). Sample postures drawn from the 95th percentile of

amplitudes are shown for the indicated PCs (right). See Fig. 4-Supp. 1 for supplemental embryos. f) A representative PC1 amplitude trace is shown for an embryo from 530 mpf until hatch (top). DV bend profiles in two 20 min windows are compared (bottom). At 610 mpf (yellow), motion is dominated by flipping between all dorsal and all ventral body bends. At 750 mpf (green), motion is dominated by dorsoventral bend propagation along the A/P axis. The corresponding PC2 and PC3 amplitudes for these time windows are shown. At 750 mpf, travelling waves are captured by phase-shifted cycling of PC2 and PC3. See Fig. 4-Supp. 2 for more embryos.

Figure 4 - Supplement 1: a) Distribution of PC1 amplitudes early (blue, 530-668 mpf) versus late (red, 669-807 mpf). Seam cell identity was assigned for each embryo to match the late positive skew seen in b). b) Distribution of PC1 amplitudes for 16 embryos with known left and right seam cell identities. c) Eigen-embryos, i.e., eigenvectors for the first 4 PCs, derived from the 16 embryos with known seam cell identities.

Figure 4 - Supplement 2: a) PC1 amplitude for 3 embryos from 530 mpf until hatch. b) DV bend profiles for 3 embryos from 530-550 mpf (left). Projection of these profiles onto 3 planes in PC space (right). c) Same as b) for 750-770 mpf.

Figure 5: *unc-13* **mutants have a late-stage motility defect.** a-b) Seam cell motions are compared in WT and *unc-13* mutant embryos at 750 mpf (a) and 530 mpf (b). Representative 10 minute trajectories for the H1 seam cell (left) and mean diffusion coefficients for all seam cell pairs (right; mean +/- SEM) are shown. Scale bar, 10 μm. Sample sizes, 750 mpf (3 WT, 3 *unc-13*); 530 mpf (3 WT, 2 *unc-13*). c) Cumulative distribution functions are shown for duration of transitions between dorsal and ventral coils (i.e., flips) from 530-540 mpf. Flip durations observed in WT and *unc-13* mutants cannot be distinguished. d) Posture transitions during flipping were unaltered in *unc-13* mutants. An embryo's transitions through posture space during flipping is compared in WT and *unc-13* mutants (530-540 mpf; only transitions executed in ≤ 10 seconds are plotted). Flips were categorized into four motifs based on the mean amplitude of PC2 and PC3 during the transition (PC2+, PC2-, PC3+, and PC3-). The start (arrowhead) and end (dot) of each flip is indicated. e) Summary of coiling transition trajectories in posture space at 530-540 mpf, with arrowhead sizes indicating the frequency of occurrence. Color-code same as in d). Schematized worms (black squiggles) are shown with ventral down and head (red dot) to the left.

Figure 6: **"Slow wave twitch" (SWT) requires cholinergic and neuropeptide signalling.** a) Brightfield twitch profiles are shown for wild-type (WT; n = 24) and *unc-13* mutants (n = 23). Each line corresponds to a single embryo. All embryos are aligned at twitch onset (430 mpf). Proportion of pixels changing intensity (smoothed over 10 seconds) is indicated by the color LUT. b) SWT behavior is absent in *unc-13* mutants. Mean twitching scalograms for wild-type and *unc-13* mutants and the difference scalogram (WT – *unc-13*) are shown. The signal in the 20-40 mHz frequency band around 660 to 720 mpf (arrow) is SWT behavior. c) The timing of peak relative power in the SWT frequency band (20-40 mHz) is plotted (mean +/- SEM, with each dot corresponding to an embryo). d) SWT behavior requires cholinergic and neuropeptide signaling. Peak SWT power ratios compared for several synaptic signalling mutants. Mean +/- SEM are shown, with each dot corresponding to an embryo. Sample sizes are as follows: WT, n=156; *cat-1* VMAT, n=11; *eat-4* VGLUT, n=24; *unc-47* VGAT, n=30; *unc-17* VAChT, n=26; *acr-16* nAChR, n=31; *unc-29* nAChR, n=29; muscle::UNC-29, n=31; *egl-3* PC2, n=17; *egl-21* CPE, n=16. One-way ANOVA and Tukey's honestly significant difference criterion were used to compare strains. Significant differences from wild-type are indicated (***, $p < 0.001$). The dashed line indicates the peak SWT power ratio derived from shuffled wild-type data. Fig. 6-Supp. 1 shows the full twitch profiles for strains with SWT defects.

Figure 6 - Supplement 1: a) Sample twitch profiles for indicated genotypes and their contemporaneous wild-type control. Top: Mean proportion of pixels changing intensity as a function of age. Bottom: Proportion of pixels changing intensity as a function of age, with each line corresponding to an embryo and aligned at twitch onset (smoothed over 10 seconds). b) Cumulative distribution functions from the brightfield assay. On a relative timeline where twitch onset is 0 and hatching is 1, "early", "mid", and "late" refer to 100 minutes centered on 0.2, 0.5, and 0.8, respectively.

Figure 7: **SWT behavior requires function of the RIS neuron.** a) The contribution of two quiescence promoting neurons (RIS and ALA) to SWT behavior is evaluated. SWT behavior is deficient in mutants lacking RIS function (*aptf-1* and *flp-11*) but is unaffected in those lacking ALA function (*ceh-17*). Left: Representative twitch traces at peak SWT power ratio are shown. Amplitudes indicate the proportion of pixels changing intensity. Right: Peak relative power in the SWT frequency band (20-40 mHz) is plotted for the indicated genotypes. Mean +/- SEM, with each dot corresponding to an embryo. The dashed line denotes peak SWT power ratio derived from shuffled data. Two *aptf-1* alleles (*gk794* and *tm3287*) were analyzed. One-way ANOVA and Tukey's honestly significant difference criterion were used to compare strains. Significant differences from wild-type are indicated (***, $p < 0.001$). b) Top: Brightfield twitch profiles are shown for wild-type (WT) and *flp-11* mutants. Each line corresponds to an individual embryo aligned at twitch onset (430 mpf). The proportion of pixels changing intensity (smoothed over 10 seconds) is indicated by the color LUT. See Fig.7-Supp. 1 for cumulative distribution functions. Bottom: Wild-type and *flp-11* scalograms. Note the SWT signature in WT (arrow) is missing in *flp-11* mutants.

Figure 7 - Supplement 1: a) Cumulative distribution functions from the brightfield assay for wild-type (WT) and *flp-11* mutants. On a relative timeline where twitch onset is 0 and hatching is 1, "early", "mid", and "late" refer to 100 minutes centered on 0.2, 0.5, and 0.8, respectively.

Video 1: Seam cell nuclei fit with a natural cubic spline from H0 (blue) to tail (yellow; left). Scale bar, 10 μm. Projection of postures onto 3 planes in PC space, with red x's denoting pauses (right). Original data acquired at 3 Hz.

Figure 8: **SWT behavior correlates with rhythmic RIS activity.** a) Time lapse images of a WT embryo expressing GCaMP (top) fused to mCherry (bottom) in RIS. A single confocal plane is shown. Time stamp, seconds. Scale bar, 10 μm b-g) RIS activity (assessed by cell body GCaMP) and embryo motion (assessed by RIS cell body displacement) were simultaneously recorded in individual embryos. b) Representative activity (top) and motion (bottom) traces are shown for WT and *flp-11* mutants. Grey bands indicate calcium transient durations (defined by widths at half peak amplitude). The green bar spans the period shown in a). Calcium transient and quiescent bout frequency c) and durations d), and calcium transient amplitudes e) are plotted. Mean +/- SEM are indicated. Each dot represents an individual embryo. Significant differences from WT (***, $p < 0.001$) were determined by an unpaired two-sample t-test. f) Traces of median normalized speed and GCaMP and mCherry intensity are aligned to calcium transient onset (Time = 0 seconds defined as the time of half peak GCaMP/mCherry ratio). Behavioral slowing was more transient in *flp-11* mutants. Behavioral slowing was not correlated with mCherry intensity, suggesting that motion artifacts cannot explain the correlation with GCaMP intensity. g) Quiescent fraction traces aligned to RIS calcium transient onset are plotted. Quiescence was defined as RIS displacement less than or equal to 0.5 μm per second for at least 3 seconds. In panels f and g, colored lines and grey shading correspond to mean +/- SD of the sampling distribution estimated by hierarchical bootstrapping for n=269 (WT) and n=261 (*flp-11*) calcium transients from n=38 and n=32 embryos, respectively. See Fig. 8-Supp. 1 for *unc-25* GAD mutant data.

Figure 8 - Supplement 1: a) Traces of median normalized speed and GCaMP and mCherry intensity aligned to calcium transient onset are shown for *unc-25* GAD mutants (Time = 0 seconds defined as the time of half peak GCaMP/mCherry ratio). b) Quiescent fraction traces aligned to RIS calcium transient onset are shown. Quiescence was defined as RIS displacement less than or equal to 0.5 μm/s for at least 3 seconds. c) Median speed change from baseline at the onset of RIS calcium transients (baseline defined as median speed over the preceding 20 seconds). In panels a-c, mean +/- SD of the sampling distribution estimated by hierarchical bootstrapping for n=327 (*unc-25*) and n=358 (*unc-25;flp-11*) calcium transients from n=46 and n=34 embryos, respectively. In panel c), asterisks indicate a group difference beyond the 99% confidence interval estimated by hierarchical bootstrapping.

Figure 9: **SWT quiescent bouts are reversible, but arousal responses are dampened by FLP-11.** A brief (10 second) UVB light stimulus transiently inhibits RIS activity and evokes aroused embryo motion. UVB evoked RIS inhibition and aroused motion were both eliminated in *lite-1* mutants, which lack the endogenous light receptor. The arousal response is apparent even when the stimulus occurs during a quiescent bout (i.e. during an RIS transient), indicating that SWT quiescence is reversible. The arousal response is prolonged in *flp-11* mutants, suggesting that light responses are dampened by RIS during SWT. Normalized GCaMP intensity and speed of the RIS cell body were simultaneously recorded in individual embryos of the indicated genotypes before, during, and after a UVB stimulus (purple bar). Trials were categorized based on the state of RIS at the onset of the stimulus (RIS$_{on}$ and RIS$_{off}$). a, c, e) Traces of RIS activity and speed are plotted (mean +/-SEM). Sample sizes are as follows: WT RIS$_{on}$, n=34; WT RIS$_{off}$, n=22; *flp-11* RIS$_{on}$, n=32; *flp-11* RIS$_{off}$, n=15; *lite-1* RIS$_{on}$, n=22; *lite-1* RIS$_{off}$, n=14 embryos. b, d, f) Mean RIS activity and speed for the time points labelled in a) ("pre", "stim", "post") are plotted. Each dot indicates an embryo. Mean +/- SEM. Data are shown for WT (a, b), *flp-11* (c, d), and *lite-1* mutants (e, f). "Pre", "stim", and "post" time points were compared using a non-parametric repeated measures test (Friedman), followed by a Dunn's multiple comparison test. Asterisks denote statistically distinguishable groups at $p < 0.001$ (***) or $p < 0.05$ (*). See Fig. 9-Supp. 1 for data from brightfield recordings.

Figure 9 - Supplement 1: a) Brightfield recording before, during, and after a single multi-wavelength light pulse (blue bar; 395 nm, 440 nm, and 470 nm peaks measured at the objective as 5.6 mW, 14.9 mW, and 13.4 mW, respectively). Lines and grey shading correspond to mean +/- SEM. n=57 (WT) and n=60 (*flp-11*) embryos. b) Mean pixel changes over the time points labelled in a) are plotted. Each dot indicates an embryo. Mean +/- SEM. Significant differences between "pre" and "post" time points (***, $p < 0.001$; *, $p < 0.05$) were determined by a non-parametric repeated measures test (Friedman).

Figure 10: *C. elegans* **embryonic behavioral maturation.** Posture (top) and movement (bottom) data derived from seam cell tracking and brightfield recordings, respectively. Temporal scaling is shown along a relative timeline to account for day-to-day differences in developmental rate (Fig. 3-Supp. 1).

References

[1] T. K. Hensch, CRITICAL PERIOD REGULATION, Annual Review of Neuroscience 27 (1) (2004) 549–579. `doi:10.1146/annurev.neuro.27.070203.144327`.
URL `http://www.annualreviews.org/doi/10.1146/annurev.neuro.27.070203.144327`

[2] W. T. Preyer, Specielle Physiologie des Embryo: Untersuchungen ueber die Lebenserscheinungen vor der Geburt, Th. Grieben's Verlag (L. Fernau), Leipzig, 1885.

[3] V. Hamburger, Some Aspects of the Embryology of Behavior, The Quarterly Review of Biology 38 (4) (1963) 342–365. `doi:10.1086/403941`.
URL `https://www.journals.uchicago.edu/doi/10.1086/403941`

[4] G. J. Berman, Measuring behavior across scales, BMC Biology 16 (1) (2018) 23. `doi:10.1186/s12915-018-0494-7`.
URL `https://bmcbiol.biomedcentral.com/articles/10.1186/s12915-018-0494-7`

[5] A. E. X. Brown, B. de Bivort, Ethology as a physical science, Nature Physics 14 (7) (2018) 653–657. `doi:10.1038/s41567-018-0093-0`.
URL `http://www.nature.com/articles/s41567-018-0093-0`

[6] S. R. Datta, D. J. Anderson, K. Branson, P. Perona, A. Leifer, Computational Neuroethology: A Call to Action, Neuron 104 (1) (2019) 11–24. `doi:10.1016/j.neuron.2019.09.038`.
URL `https://linkinghub.elsevier.com/retrieve/pii/S0896627319308414`

[7] T. D. Pereira, J. W. Shaevitz, M. Murthy, Quantifying behavior to understand the brain, Nature Neuroscience 23 (12) (2020) 1537–1549. `doi:10.1038/s41593-020-00734-z`.
URL `http://www.nature.com/articles/s41593-020-00734-z`

[8] P. K. Shah, M. R. Tanner, I. Kovacevic, A. Rankin, T. E. Marshall, N. Noblett, N. N. Tran, T. Roenspies, J. Hung, Z. Chen, C. Slatculescu, T. J. Perkins, Z. Bao, A. Colavita, PCP and SAX-3/Robo Pathways Cooperate to Regulate Convergent Extension-Based Nerve Cord Assembly in C. elegans, Developmental Cell 41 (2) (2017) 195–203.e3. `doi:10.1016/j.devcel.2017.03.024`.
URL `https://linkinghub.elsevier.com/retrieve/pii/S1534580717302101`

[9] K. M. Barnes, L. Fan, M. W. Moyle, C. A. Brittin, Y. Xu, D. A. Colón-Ramos, A. Santella, Z. Bao, Cadherin preserves cohesion across involuting tissues during C. elegans neurulation, eLife 9 (Oct. 2020). `doi:10.7554/eLife.58626`.
URL `https://elifesciences.org/articles/58626`

[10] M. G. Heiman, S. Shaham, DEX-1 and DYF-7 Establish Sensory Dendrite Length by Anchoring Dendritic Tips during Cell Migration, Cell 137 (2) (2009) 344–355. `doi:10.1016/j.cell.2009.01.057`.
URL `https://linkinghub.elsevier.com/retrieve/pii/S0092867409001597`

[11] L. Fan, I. Kovacevic, M. G. Heiman, Z. Bao, A multicellular rosette-mediated collective dendrite extension, eLife 8 (2019) e38065. `doi:10.7554/eLife.38065`.
URL `https://elifesciences.org/articles/38065`

[12] R. P. Christensen, A. Bokinsky, A. Santella, Y. Wu, J. Marquina-Solis, M. Guo, I. Kovacevic, A. Kumar, P. W. Winter, N. Tashakkori, E. McCreedy, H. Liu, M. McAuliffe, W. Mohler, D. A. Colón-Ramos, Z. Bao, H. Shroff, Untwisting the Caenorhabditis elegans embryo, eLife 4 (2015) e10070, publisher: eLife Sciences Publications, Ltd. `doi:10.7554/eLife.10070`.
URL `https://doi.org/10.7554/eLife.10070`

[13] M. W. Moyle, K. M. Barnes, M. Kuchroo, A. Gonopolskiy, L. H. Duncan, T. Sengupta, L. Shao, M. Guo, A. Santella, R. Christensen, A. Kumar, Y. Wu, K. R. Moon, G. Wolf, S. Krishnaswamy, Z. Bao, H. Shroff, W. A. Mohler, D. A. Colón-Ramos, Structural and developmental principles of neuropil assembly in C. elegans, Nature 591 (7848) (2021) 99–104. `doi:10.1038/s41586-020-03169-5`.
URL `http://www.nature.com/articles/s41586-020-03169-5`

[14] N. A. McDonald, R. D. Fetter, K. Shen, Assembly of synaptic active zones requires phase separation of scaffold molecules, Nature 588 (7838) (2020) 454–458. `doi:10.1038/s41586-020-2942-0`.
URL `http://www.nature.com/articles/s41586-020-2942-0`

[15] T. Sengupta, N. L. Koonce, M. W. Moyle, L. H. Duncan, N. Vázquez-Martínez, S. E. Emerson, X. Han, L. Shao, Y. Wu, A. Santella, L. Fan, Z. Bao, W. A. Mohler, H. Shroff, D. A. Colón-Ramos, Differential adhesion regulates neurite placement via a retrograde zippering mechanism, Tech. rep. (Jun. 2021).
URL `https://www.biorxiv.org/content/10.1101/2020.08.28.271437v2`

[16] E. L. Ardiel, A. Kumar, J. Marbach, R. Christensen, R. Gupta, W. Duncan, J. S. Daniels, N. Stuurman, D. Colón-Ramos, H. Shroff, Visualizing Calcium Flux in Freely Moving Nematode Embryos, Biophysical Journal 112 (9) (2017) 1975–1983. doi:10.1016/j.bpj.2017.02.035.

[17] D. H. Hall, E. M. Hedgecock, Kinesin-related gene unc-104 is required for axonal transport of synaptic vesicles in C. elegans, Cell 65 (5) (1991) 837–847. doi:10.1016/0092-8674(91)90391-B.
URL https://linkinghub.elsevier.com/retrieve/pii/009286749190391B

[18] H. Baris Atakan, T. Alkanat, M. Cornaglia, R. Trouillon, M. A. M. Gijs, Automated phenotyping of Caenorhabditis elegans embryos with a high-throughput-screening microfluidic platform, Microsystems & Nanoengineering 6 (1) (2020) 1–14, number: 1 Publisher: Nature Publishing Group. doi:10.1038/s41378-020-0132-8.
URL https://www.nature.com/articles/s41378-020-0132-8

[19] E. A. Bayer, K. M. Liberatore, J. R. Schneider, E. Schlesinger, Z. He, S. Birnbaum, B. Wightman, Insulin signaling and osmotic stress response regulate arousal and developmental progression of C. elegans at hatching, Genetics (iyab202) (Nov. 2021). doi:10.1093/genetics/iyab202.
URL https://doi.org/10.1093/genetics/iyab202

[20] J. G. White, E. Southgate, J. N. Thomson, S. Brenner, The structure of the nervous system of the nematode Caenorhabditis elegans, Philosophical Transactions of the Royal Society of London. B, Biological Sciences 314 (1165) (1986) 1–340, publisher: Royal Society. doi:10.1098/rstb.1986.0056.
URL https://royalsocietypublishing.org/doi/10.1098/rstb.1986.0056

[21] S. J. Cook, T. A. Jarrell, C. A. Brittin, Y. Wang, A. E. Bloniarz, M. A. Yakovlev, K. C. Q. Nguyen, L. T.-H. Tang, E. A. Bayer, J. S. Duerr, H. E. Bülow, O. Hobert, D. H. Hall, S. W. Emmons, Whole-animal connectomes of both Caenorhabditis elegans sexes, Nature 571 (7763) (2019) 63–71. doi:10.1038/s41586-019-1352-7.

[22] D. Witvliet, B. Mulcahy, J. K. Mitchell, Y. Meirovitch, D. R. Berger, Y. Wu, Y. Liu, W. X. Koh, R. Parvathala, D. Holmyard, R. L. Schalek, N. Shavit, A. D. Chisholm, J. W. Lichtman, A. D. T. Samuel, M. Zhen, Connectomes across development reveal principles of brain maturation, Nature 596 (7871) (2021) 257–261. doi:10.1038/s41586-021-03778-8.

[23] J. S. Packer, Q. Zhu, C. Huynh, P. Sivaramakrishnan, E. Preston, H. Dueck, D. Stefanik, K. Tan, C. Trapnell, J. Kim, R. H. Waterston, J. I. Murray, A lineage-resolved molecular atlas of C. elegans embryogenesis at single-cell resolution, Science (New York, N.Y.) 365 (6459) (2019) eaax1971. doi:10.1126/science.aax1971.

[24] S. Stern, C. Kirst, C. I. Bargmann, Neuromodulatory Control of Long-Term Behavioral Patterns and Individuality across Development, Cell 171 (7) (2017) 1649–1662.e10. doi:10.1016/j.cell.2017.10.041.

[25] M. A. Churgin, S.-K. Jung, C.-C. Yu, X. Chen, D. M. Raizen, C. Fang-Yen, Longitudinal imaging of Caenorhabditis elegans in a microfabricated device reveals variation in behavioral decline during aging, eLife 6 (2017) e26652. doi:10.7554/eLife.26652.

[26] Z. Bao, J. I. Murray, T. Boyle, S. L. Ooi, M. J. Sandel, R. H. Waterston, Automated cell lineage tracing in Caenorhabditis elegans, Proceedings of the National Academy of Sciences of the United States of America 103 (8) (2006) 2707–2712. doi:10.1073/pnas.0511111103.

[27] C. A. Giurumescu, S. Kang, T. A. Planchon, E. Betzig, J. Bloomekatz, D. Yelon, P. Cosman, A. D. Chisholm, Quantitative semi-automated analysis of morphogenesis with single-cell resolution in complex embryos, Development (Cambridge, England) 139 (22) (2012) 4271–4279. doi:10.1242/dev.086256.

[28] A. Kumar, R. Christensen, M. Guo, P. Chandris, W. Duncan, Y. Wu, A. Santella, M. Moyle, P. W. Winter, D. Colón-Ramos, Z. Bao, H. Shroff, Using Stage- and Slit-Scanning to Improve Contrast and Optical Sectioning in Dual-View Inverted Light Sheet Microscopy (diSPIM), The Biological Bulletin 231 (1) (2016) 26–39. doi:10.1086/689589.

[29] M. Hong, L. Ryu, M. C. Ow, J. Kim, A. R. Je, S. Chinta, Y. H. Huh, K. J. Lee, R. A. Butcher, H. Choi, P. Sengupta, S. E. Hall, K. Kim, Early Pheromone Experience Modifies a Synaptic Activity to Influence Adult Pheromone Responses of C. elegans, Current biology: CB 27 (20) (2017) 3168–3177.e3. doi:10.1016/j.cub.2017.08.068.

[30] B. D. Williams, R. H. Waterston, Genes critical for muscle development and function in Caenorhabditis elegans identified through lethal mutations, The Journal of Cell Biology 124 (4) (1994) 475–490. doi:10.1083/jcb.124.4.475.

[31] R. Durbin, Thesis Part I (1987).
URL https://www.wormatlas.org/Durbin/Durbin1987partI.html

[32] M. Turek, J. Besseling, J.-P. Spies, S. König, H. Bringmann, Sleep-active neuron specification and sleep induction require FLP-11 neuropeptides to systemically induce sleep, eLife 5 (Mar. 2016). `doi:10.7554/eLife.12499`.

[33] Y. Wu, F. Masurat, J. Preis, H. Bringmann, Sleep Counteracts Aging Phenotypes to Survive Starvation-Induced Developmental Arrest in C. elegans, Current biology: CB 28 (22) (2018) 3610–3624.e8. `doi:10.1016/j.cub.2018.10.009`.

[34] E. Balaban, M. Desco, J.-J. Vaquero, Waking-like Brain Function in Embryos, Current Biology 22 (10) (2012) 852–861. `doi:10.1016/j.cub.2012.03.030`.
URL `https://www.sciencedirect.com/science/article/pii/S096098221200317X`

[35] W. Pereanu, S. Spindler, E. Im, N. Buu, V. Hartenstein, The emergence of patterned movement during late embryogenesis of Drosophila, Developmental Neurobiology 67 (12) (2007) 1669–1685. `doi:10.1002/dneu.20538`.

[36] T. Okai, S. Kozuma, N. Shinozuka, Y. Kuwabara, M. Mizuno, A study on the development of sleep-wakefulness cycle in the human fetus, Early Human Development 29 (1) (1992) 391–396. `doi:10.1016/0378-3782(92)90198-p`.

[37] H. H. Szeto, D. J. Hinman, Prenatal development of sleep-wake patterns in sheep, Sleep 8 (4) (1985) 347–355. `doi:10.1093/sleep/8.4.347`.

[38] M. A. Corner, Sleep and the beginnings of behavior in the animal kingdom–studies of ultradian motility cycles in early life, Progress in Neurobiology 8 (4) (1977) 279–295. `doi:10.1016/0301-0082(77)90008-9`.

[39] Y. Wu, P. Wawrzusin, J. Senseney, R. S. Fischer, R. Christensen, A. Santella, A. G. York, P. W. Winter, C. M. Waterman, Z. Bao, D. A. Colón-Ramos, M. McAuliffe, H. Shroff, Spatially isotropic four-dimensional imaging with dual-view plane illumination microscopy, Nature Biotechnology 31 (11) (2013) 1032–1038, number: 11 Publisher: Nature Publishing Group. `doi:10.1038/nbt.2713`.
URL `https://www.nature.com/articles/nbt.2713`

[40] A. Kumar, Y. Wu, R. Christensen, P. Chandris, W. Gandler, E. McCreedy, A. Bokinsky, D. A. Colón-Ramos, Z. Bao, M. McAuliffe, G. Rondeau, H. Shroff, Dual-view plane illumination microscopy for rapid and spatially isotropic imaging, Nature Protocols 9 (11) (2014) 2555–2573. `doi:10.1038/nprot.2014.172`.

[41] O. Ronneberger, P. Fischer, T. Brox, U-Net: Convolutional Networks for Biomedical Image Segmentation, in: N. Navab, J. Hornegger, W. M. Wells, A. F. Frangi (Eds.), Medical Image Computing and Computer-Assisted Intervention – MICCAI 2015, Lecture Notes in Computer Science, Springer International Publishing, Cham, 2015, pp. 234–241. `doi:10.1007/978-3-319-24574-4_28`.

[42] Çiçek, A. Abdulkadir, S. S. Lienkamp, T. Brox, O. Ronneberger, 3D U-Net: Learning Dense Volumetric Segmentation from Sparse Annotation, in: S. Ourselin, L. Joskowicz, M. R. Sabuncu, G. Unal, W. Wells (Eds.), Medical Image Computing and Computer-Assisted Intervention – MICCAI 2016, Lecture Notes in Computer Science, Springer International Publishing, Cham, 2016, pp. 424–432.

[43] T. Lindeberg, Feature Detection with Automatic Scale Selection, International Journal of Computer Vision 30 (2) (1998) 79–116. `doi:10.1023/A:1008045108935`.
URL `https://doi.org/10.1023/A:1008045108935`

[44] D. G. Lowe, Distinctive Image Features from Scale-Invariant Keypoints, International Journal of Computer Vision 60 (2) (2004) 91–110. `doi:10.1023/B:VISI.0000029664.99615.94`.
URL `https://doi.org/10.1023/B:VISI.0000029664.99615.94`

[45] J.-Y. Tinevez, N. Perry, J. Schindelin, G. M. Hoopes, G. D. Reynolds, E. Laplantine, S. Y. Bednarek, S. L. Shorte, K. W. Eliceiri, TrackMate: An open and extensible platform for single-particle tracking, Methods 115 (2017) 80–90. `doi:10.1016/j.ymeth.2016.09.016`.
URL `http://www.sciencedirect.com/science/article/pii/S1046202316303346`

[46] W. Luo, J. Xing, A. Milan, X. Zhang, W. Liu, T.-K. Kim, Multiple object tracking: A literature review, Artificial Intelligence 293 (2021) 103448. `doi:10.1016/j.artint.2020.103448`.
URL `https://www.sciencedirect.com/science/article/pii/S0004370220301958`

[47] D. Reid, An algorithm for tracking multiple targets, IEEE Transactions on Automatic Control 24 (6) (1979) 843–854, conference Name: IEEE Transactions on Automatic Control. `doi:10.1109/TAC.1979.1102177`.

[48] S. S. Blackman, Multiple hypothesis tracking for multiple target tracking, IEEE Aerospace and Electronic Systems Magazine 19 (1) (2004) 5–18, conference Name: IEEE Aerospace and Electronic Systems Magazine. `doi:10.1109/MAES.2004.1263228`.

[49] I. J. Cox, S. L. Hingorani, An efficient implementation of Reid's multiple hypothesis tracking algorithm and its evaluation for the purpose of visual tracking, IEEE Transactions on Pattern Analysis and Machine Intelligence 18 (2) (1996) 138–150, conference Name: IEEE Transactions on Pattern Analysis and Machine Intelligence. doi:10.1109/34.481539.

[50] A. Lauziere, E. Ardiel, S. Xu, H. Shroff, Multiple Hypothesis Hypergraph Tracking for Posture Identification in Embryonic Caenorhabditis elegans, arXiv:2111.06425 [cs, eess, q-bio]ArXiv: 2111.06425 (Nov. 2021).
URL http://arxiv.org/abs/2111.06425

[51] W. Wood, The Nematode Caenorhabditis elegans, Cold Spring Harbor Laboratory Press, New York, 1988.

[52] G. J. Stephens, B. Johnson-Kerner, W. Bialek, W. S. Ryu, Dimensionality and dynamics in the behavior of C. elegans, PLoS computational biology 4 (4) (2008) e1000028. doi:10.1371/journal.pcbi.1000028.

[53] J. G. White, D. G. Albertson, M. A. Anness, Connectivity changes in a class of motoneurone during the development of a nematode, Nature 271 (5647) (1978) 764–766. doi:10.1038/271764a0.

[54] S. J. Hallam, Y. Jin, lin-14 regulates the timing of synaptic remodelling in Caenorhabditis elegans, Nature 395 (6697) (1998) 78–82. doi:10.1038/25757.

[55] W. W. Walthall, L. Li, J. A. Plunkett, C.-Y. Hsu, Changing synaptic specificities in the nervous system of Caenorhabditis elegans: Differentiation of the DD motoneurons, Journal of Neurobiology 24 (12) (1993) 1589–1599, _eprint: https://onlinelibrary.wiley.com/doi/pdf/10.1002/neu.480241204. doi:10.1002/neu.480241204.
URL https://onlinelibrary.wiley.com/doi/abs/10.1002/neu.480241204

[56] J. E. Richmond, E. M. Jorgensen, One GABA and two acetylcholine receptors function at the C. elegans neuromuscular junction, Nature Neuroscience 2 (9) (1999) 791–797. doi:10.1038/12160.

[57] D. Touroutine, R. M. Fox, S. E. Von Stetina, A. Burdina, D. M. Miller, J. E. Richmond, acr-16 encodes an essential subunit of the levamisole-resistant nicotinic receptor at the Caenorhabditis elegans neuromuscular junction, The Journal of Biological Chemistry 280 (29) (2005) 27013–27021. doi:10.1074/jbc.M502818200.

[58] M. Turek, I. Lewandrowski, H. Bringmann, An AP2 transcription factor is required for a sleep-active neuron to induce sleep-like quiescence in C. elegans, Current biology: CB 23 (22) (2013) 2215–2223. doi:10.1016/j.cub.2013.09.028.

[59] C. Van Buskirk, P. W. Sternberg, Epidermal growth factor signaling induces behavioral quiescence in Caenorhabditis elegans, Nature Neuroscience 10 (10) (2007) 1300–1307. doi:10.1038/nn1981.

[60] R. D. Nath, E. S. Chow, H. Wang, E. M. Schwarz, P. W. Sternberg, C. elegans Stress-Induced Sleep Emerges from the Collective Action of Multiple Neuropeptides, Current biology: CB 26 (18) (2016) 2446–2455. doi:10.1016/j.cub.2016.07.048.

[61] N. Pujol, P. Torregrossa, J. J. Ewbank, J. F. Brunet, The homeodomain protein CePHOX2/CEH-17 controls antero-posterior axonal growth in C. elegans, Development (Cambridge, England) 127 (15) (2000) 3361–3371.

[62] Z. Chen, M. Hendricks, A. Cornils, W. Maier, J. Alcedo, Y. Zhang, Two insulin-like peptides antagonistically regulate aversive olfactory learning in C. elegans, Neuron 77 (3) (2013) 572–585. doi:10.1016/j.neuron.2012.11.025.

[63] S. L. Edwards, N. K. Charlie, M. C. Milfort, B. S. Brown, C. N. Gravlin, J. E. Knecht, K. G. Miller, A Novel Molecular Solution for Ultraviolet Light Detection in Caenorhabditis elegans, PLOS Biology 6 (8) (2008) e198, publisher: Public Library of Science. doi:10.1371/journal.pbio.0060198.
URL https://journals.plos.org/plosbiology/article?id=10.1371/journal.pbio.0060198

[64] J. Liu, A. Ward, J. Gao, Y. Dong, N. Nishio, H. Inada, L. Kang, Y. Yu, D. Ma, T. Xu, I. Mori, Z. Xie, X. Z. S. Xu, C. elegans phototransduction requires a G protein–dependent cGMP pathway and a taste receptor homolog, Nature Neuroscience 13 (6) (2010) 715–722, number: 6 Publisher: Nature Publishing Group. doi:10.1038/nn.2540.
URL https://www.nature.com/articles/nn.2540

[65] J. Gong, Y. Yuan, A. Ward, L. Kang, B. Zhang, Z. Wu, J. Peng, Z. Feng, J. Liu, X. Z. S. Xu, The C. elegans Taste Receptor Homolog LITE-1 Is a Photoreceptor, Cell 167 (5) (2016) 1252–1263.e10, publisher: Elsevier. doi:10.1016/j.cell.2016.10.053.
URL https://www.cell.com/cell/abstract/S0092-8674(16)31518-5

[66] J. R. Priess, D. I. Hirsh, Caenorhabditis elegans morphogenesis: the role of the cytoskeleton in elongation of the embryo, Developmental Biology 117 (1) (1986) 156–173. doi:10.1016/0012-1606(86)90358-1.

[67] D. M. Raizen, J. E. Zimmerman, M. H. Maycock, U. D. Ta, Y.-j. You, M. V. Sundaram, A. I. Pack, Lethargus is a Caenorhabditis elegans sleep-like state, Nature 451 (7178) (2008) 569–572. doi:10.1038/nature06535.

[68] Y.-j. You, J. Kim, D. M. Raizen, L. Avery, Insulin, cGMP, and TGF-beta signals regulate food intake and quiescence in C. elegans: a model for satiety, Cell Metabolism 7 (3) (2008) 249–257. doi:10.1016/j.cmet.2008.01.005.

[69] A. J. Hill, R. Mansfield, J. M. N. G. Lopez, D. M. Raizen, C. Van Buskirk, Cellular stress induces a protective sleep-like state in C. elegans, Current biology: CB 24 (20) (2014) 2399–2405. doi:10.1016/j.cub.2014.08.040.

[70] M. D. Nelson, K. H. Lee, M. A. Churgin, A. J. Hill, C. Van Buskirk, C. Fang-Yen, D. M. Raizen, FMRFamide-like FLP-13 Neuropeptides Promote Quiescence following Heat Stress in Caenorhabditis elegans, Current Biology 24 (20) (2014) 2406–2410, publisher: Elsevier. doi:10.1016/j.cub.2014.08.037.
URL https://www.cell.com/current-biology/abstract/S0960-9822(14)01050-1

[71] S. Skora, F. Mende, M. Zimmer, Energy Scarcity Promotes a Brain-wide Sleep State Modulated by Insulin Signaling in C. elegans, Cell Reports 22 (4) (2018) 953–966. doi:10.1016/j.celrep.2017.12.091.

[72] D. L. Gonzales, J. Zhou, B. Fan, J. T. Robinson, A microfluidic-induced C. elegans sleep state, Nature Communications 10 (1) (2019) 5035. doi:10.1038/s41467-019-13008-5.

[73] S. Choi, M. Chatzigeorgiou, K. P. Taylor, W. R. Schafer, J. M. Kaplan, Analysis of NPR-1 reveals a circuit mechanism for behavioral quiescence in C. elegans, Neuron 78 (5) (2013) 869–880. doi:10.1016/j.neuron.2013.04.002.

[74] S. Iwanir, N. Tramm, S. Nagy, C. Wright, D. Ish, D. Biron, The microarchitecture of C. elegans behavior during lethargus: homeostatic bout dynamics, a typical body posture, and regulation by a central neuron, Sleep 36 (3) (2013) 385–395. doi:10.5665/sleep.2456.

[75] J. Y. Cho, P. W. Sternberg, Multilevel Modulation of a Sensory Motor Circuit during C. elegans Sleep and Arousal, Cell 156 (1) (2014) 249–260. doi:10.1016/j.cell.2013.11.036.
URL https://www.cell.com/cell/abstract/S0092-8674(13)01520-1

[76] N. Tramm, N. Oppenheimer, S. Nagy, E. Efrati, D. Biron, Why do sleeping nematodes adopt a hockey-stick-like posture?, PloS One 9 (7) (2014) e101162. doi:10.1371/journal.pone.0101162.

[77] S. Nagy, N. Tramm, J. Sanders, S. Iwanir, I. A. Shirley, E. Levine, D. Biron, Homeostasis in C. elegans sleep is characterized by two behaviorally and genetically distinct mechanisms, eLife 3 (2014) e04380, publisher: eLife Sciences Publications, Ltd. doi:10.7554/eLife.04380.
URL https://doi.org/10.7554/eLife.04380

[78] J. Schwarz, H. Bringmann, Analysis of the NK2 homeobox gene ceh-24 reveals sublateral motor neuron control of left-right turning during sleep, eLife 6 (2017) e24846. doi:10.7554/eLife.24846.

[79] R. J. Konopka, S. Benzer, Clock mutants of Drosophila melanogaster, Proceedings of the National Academy of Sciences of the United States of America 68 (9) (1971) 2112–2116. doi:10.1073/pnas.68.9.2112.

[80] P. E. Hardin, J. C. Hall, M. Rosbash, Feedback of the Drosophila period gene product on circadian cycling of its messenger RNA levels, Nature 343 (6258) (1990) 536–540. doi:10.1038/343536a0.

[81] Z. S. Sun, U. Albrecht, O. Zhuchenko, J. Bailey, G. Eichele, C. C. Lee, RIGUI, a putative mammalian ortholog of the Drosophila period gene, Cell 90 (6) (1997) 1003–1011. doi:10.1016/s0092-8674(00)80366-9.

[82] H. Tei, H. Okamura, Y. Shigeyoshi, C. Fukuhara, R. Ozawa, M. Hirose, Y. Sakaki, Circadian oscillation of a mammalian homologue of the Drosophila period gene, Nature 389 (6650) (1997) 512–516. doi:10.1038/39086.

[83] G. C. Monsalve, C. Van Buskirk, A. R. Frand, LIN-42/PERIOD controls cyclical and developmental progression of C. elegans molts, Current biology: CB 21 (24) (2011) 2033–2045. doi:10.1016/j.cub.2011.10.054.

[84] A. Mani, J. Radhakrishnan, A. Farhi, K. S. Carew, C. A. Warnes, C. Nelson-Williams, R. W. Day, B. Pober, M. W. State, R. P. Lifton, Syndromic patent ductus arteriosus: evidence for haploinsufficient TFAP2B mutations and identification of a linked sleep disorder, Proceedings of the National Academy of Sciences of the United States of America 102 (8) (2005) 2975–2979. doi:10.1073/pnas.0409852102.

[85] M. M. Kucherenko, V. Ilangovan, B. Herzig, H. R. Shcherbata, H. Bringmann, TfAP-2 is required for night sleep in Drosophila, BMC neuroscience 17 (1) (2016) 72. doi:10.1186/s12868-016-0306-3.

[86] Y. Hu, A. Korovaichuk, M. Astiz, H. Schroeder, R. Islam, J. Barrenetxea, A. Fischer, H. Oster, H. Bringmann, Functional Divergence of Mammalian TFAP2a and TFAP2b Transcription Factors for Bidirectional Sleep Control, Genetics 216 (3) (2020) 735–752. doi:10.1534/genetics.120.303533.

[87] M. W. Meeuse, Y. P. Hauser, L. J. Morales Moya, G.-J. Hendriks, J. Eglinger, G. Bogaarts, C. Tsiairis, H. Großhans, Developmental function and state transitions of a gene expression oscillator in Caenorhabditis elegans, Molecular Systems Biology 16 (7) (2020) e9498. doi:10.15252/msb.20209498.

[88] L. A. Kirkby, G. S. Sack, A. Firl, M. B. Feller, A role for correlated spontaneous activity in the assembly of neural circuits, Neuron 80 (5) (2013) 1129–1144. doi:10.1016/j.neuron.2013.10.030.

[89] S. Crisp, J. F. Evers, A. Fiala, M. Bate, The development of motor coordination in Drosophilaembryos, Development 135 (22) (2008) 3707–3717. doi:10.1242/dev.026773.
URL https://doi.org/10.1242/dev.026773

[90] A. Carreira-Rosario, R. A. York, M. Choi, C. Q. Doe, T. R. Clandinin, Mechanosensory input during circuit formation shapes Drosophila motor behavior through patterned spontaneous network activity, Current Biology (2021) S096098222101126Xdoi:10.1016/j.cub.2021.08.022.
URL https://linkinghub.elsevier.com/retrieve/pii/S096098222101126X

[91] S. J. Crisp, J. F. Evers, M. Bate, Endogenous patterns of activity are required for the maturation of a motor network, The Journal of Neuroscience: The Official Journal of the Society for Neuroscience 31 (29) (2011) 10445–10450. doi:10.1523/JNEUROSCI.0346-11.2011.

[92] J. Sanders, M. Scholz, I. Merutka, D. Biron, Distinct unfolded protein responses mitigate or mediate effects of nonlethal deprivation of C. elegans sleep in different tissues, BMC biology 15 (1) (2017) 67. doi:10.1186/s12915-017-0407-1.

[93] P. J. Shaw, C. Cirelli, R. J. Greenspan, G. Tononi, Correlates of sleep and waking in Drosophila melanogaster, Science (New York, N.Y.) 287 (5459) (2000) 1834–1837. doi:10.1126/science.287.5459.1834.

[94] C. Cirelli, Cellular consequences of sleep deprivation in the brain, Sleep Medicine Reviews 10 (5) (2006) 307–321. doi:10.1016/j.smrv.2006.04.001.

[95] A. Terao, T. L. Steininger, K. Hyder, A. Apte-Deshpande, J. Ding, D. Rishipathak, R. W. Davis, H. C. Heller, T. S. Kilduff, Differential increase in the expression of heat shock protein family members during sleep deprivation and during sleep, Neuroscience 116 (1) (2003) 187–200. doi:10.1016/s0306-4522(02)00695-4.

[96] N. Naidoo, W. Giang, R. J. Galante, A. I. Pack, Sleep deprivation induces the unfolded protein response in mouse cerebral cortex, Journal of Neurochemistry 92 (5) (2005) 1150–1157. doi:10.1111/j.1471-4159.2004.02952.x.

[97] J. A. Lewis, C.-H. Wu, H. Berg, J. H. Levine, THE GENETICS OF LEVAMISOLE RESISTANCE IN THE NEMATODE CAENORHABDITIS ELEGANS, Genetics 95 (4) (1980) 905–928. doi:10.1093/genetics/95.4.905.
URL https://doi.org/10.1093/genetics/95.4.905

[98] S. Brenner, The genetics of Caenorhabditis elegans, Genetics 77 (1) (1974) 71–94.

[99] C. Frøkjær-Jensen, M. W. Davis, M. Sarov, J. Taylor, S. Flibotte, M. LaBella, A. Pozniakovsky, D. G. Moerman, E. M. Jorgensen, Random and targeted transgene insertion in Caenorhabditis elegans using a modified Mos1 transposon, Nature Methods 11 (5) (2014) 529–534. doi:10.1038/nmeth.2889.

[100] L. H. Duncan, M. W. Moyle, L. Shao, T. Sengupta, R. Ikegami, A. Kumar, M. Guo, R. Christensen, A. Santella, Z. Bao, H. Shroff, W. Mohler, D. A. Colón-Ramos, Isotropic Light-Sheet Microscopy and Automated Cell Lineage Analyses to Catalogue Caenorhabditis elegans Embryogenesis with Subcellular Resolution, Journal of Visualized Experiments: JoVE (148) (Jun. 2019). doi:10.3791/59533.

[101] M. Guo, Y. Li, Y. Su, T. Lambert, D. D. Nogare, M. W. Moyle, L. H. Duncan, R. Ikegami, A. Santella, I. Rey-Suarez, D. Green, A. Beiriger, J. Chen, H. Vishwasrao, S. Ganesan, V. Prince, J. C. Waters, C. M. Annunziata, M. Hafner, W. A. Mohler, A. B. Chitnis, A. Upadhyaya, T. B. Usdin, Z. Bao, D. Colón-Ramos, P. La Riviere, H. Liu, Y. Wu, H. Shroff, Rapid image deconvolution and multiview fusion for optical microscopy, Nature Biotechnology 38 (11) (2020) 1337–1346. doi:10.1038/s41587-020-0560-x.

[102] N. Tarantino, J.-Y. Tinevez, E. F. Crowell, B. Boisson, R. Henriques, M. Mhlanga, F. Agou, A. Israël, E. Laplantine, TNF and IL-1 exhibit distinct ubiquitin requirements for inducing NEMO–IKK supramolecular structures, Journal of Cell Biology 204 (2) (2014) 231–245. doi:10.1083/jcb.201307172.
URL https://doi.org/10.1083/jcb.201307172

[103] A. Falcao, J. Stolfi, R. de Alencar Lotufo, The image foresting transform: theory, algorithms, and applications, IEEE Transactions on Pattern Analysis and Machine Intelligence 26 (1) (2004) 19–29, conference Name: IEEE Transactions on Pattern Analysis and Machine Intelligence. doi:10.1109/TPAMI.2004.1261076.

[104] K. He, G. Gkioxari, P. Dollár, R. Girshick, Mask R-CNN, in: 2017 IEEE International Conference on Computer Vision (ICCV), 2017, pp. 2980–2988, iSSN: 2380-7504. doi:10.1109/ICCV.2017.322.

[105] M. Weigert, U. Schmidt, R. Haase, K. Sugawara, G. Myers, Star-convex Polyhedra for 3D Object Detection and Segmentation in Microscopy, in: 2020 IEEE Winter Conference on Applications of Computer Vision (WACV), IEEE, Snowmass Village, CO, USA, 2020, pp. 3655–3662. doi:10.1109/WACV45572.2020.9093435. URL https://ieeexplore.ieee.org/document/9093435/

[106] T. Scherr, A. Bartschat, M. Resichl, J. Stegmaier, R. Mikut, Best Practices in Deep Learning-Based Segmentation of Microscopy Images, in: Proceedings 28, Dortmund, Germany, 2018, pp. 175–195.

[107] D. P. Kingma, J. Ba, Adam: A Method for Stochastic Optimization, arXiv:1412.6980 [cs]ArXiv: 1412.6980 (Jan. 2017). URL http://arxiv.org/abs/1412.6980

[108] L. Feng, Y. Xu, Y. Yang, X. Zheng, Multiple dense particle tracking in fluorescence microscopy images based on multidimensional assignment, Journal of Structural Biology 173 (2) (2011) 219–228. doi:10.1016/j.jsb.2010.11.001. URL http://www.sciencedirect.com/science/article/pii/S1047847710003382

[109] N. Chenouard, I. Bloch, J. Olivo-Marin, Multiple Hypothesis Tracking for Cluttered Biological Image Sequences, IEEE Transactions on Pattern Analysis and Machine Intelligence 35 (11) (2013) 2736–3750, conference Name: IEEE Transactions on Pattern Analysis and Machine Intelligence. doi:10.1109/TPAMI.2013.97.

[110] K. G. Murty, An Algorithm for Ranking all the Assignments in Order of Increasing Cost, Operations Research 16 (3) (1968) 682–687. URL http://www.jstor.org/stable/168595

[111] I. Cox, M. Miller, On finding ranked assignments with application to multitarget tracking and motion correspondence, IEEE Transactions on Aerospace and Electronic Systems 31 (1) (1995) 486–489. doi:10.1109/7.366332. URL http://ieeexplore.ieee.org/document/366332/

[112] B. Lombardot, Interactive Watershed, section: Segmentation (May 2017). URL https://github.com/mpicbg-scicomp/Interactive-H-Watershed/

[113] J.-C. Olivo-Marin, Extraction of spots in biological images using multiscale products, Pattern Recognition 35 (9) (2002) 1989–1996. doi:10.1016/S0031-3203(01)00127-3. URL https://www.sciencedirect.com/science/article/pii/S0031320301001273

[114] F. de Chaumont, S. Dallongeville, N. Chenouard, N. Hervé, S. Pop, T. Provoost, V. Meas-Yedid, P. Pankajakshan, T. Lecomte, Y. Le Montagner, T. Lagache, A. Dufour, J.-C. Olivo-Marin, Icy: an open bioimage informatics platform for extended reproducible research, Nature Methods 9 (7) (2012) 690–696, bandiera_abtest: a Cg_type: Nature Research Journals Number: 7 Primary_atype: Reviews Publisher: Nature Publishing Group Subject_term: Bioinformatics;Imaging Subject_term_id: bioinformatics;imaging. doi:10.1038/nmeth.2075. URL https://www.nature.com/articles/nmeth.2075

[115] A. Waleed, Mask R-CNN for object detection and instance segmentation on Keras and TensorFlow (2017). URL https://github.com/matterport/Mask_RCNN

[116] F. Chollet, Keras: Deep Learning for humans, original-date: 2015-03-28T00:35:42Z (Sep. 2021). URL https://github.com/keras-team/keras

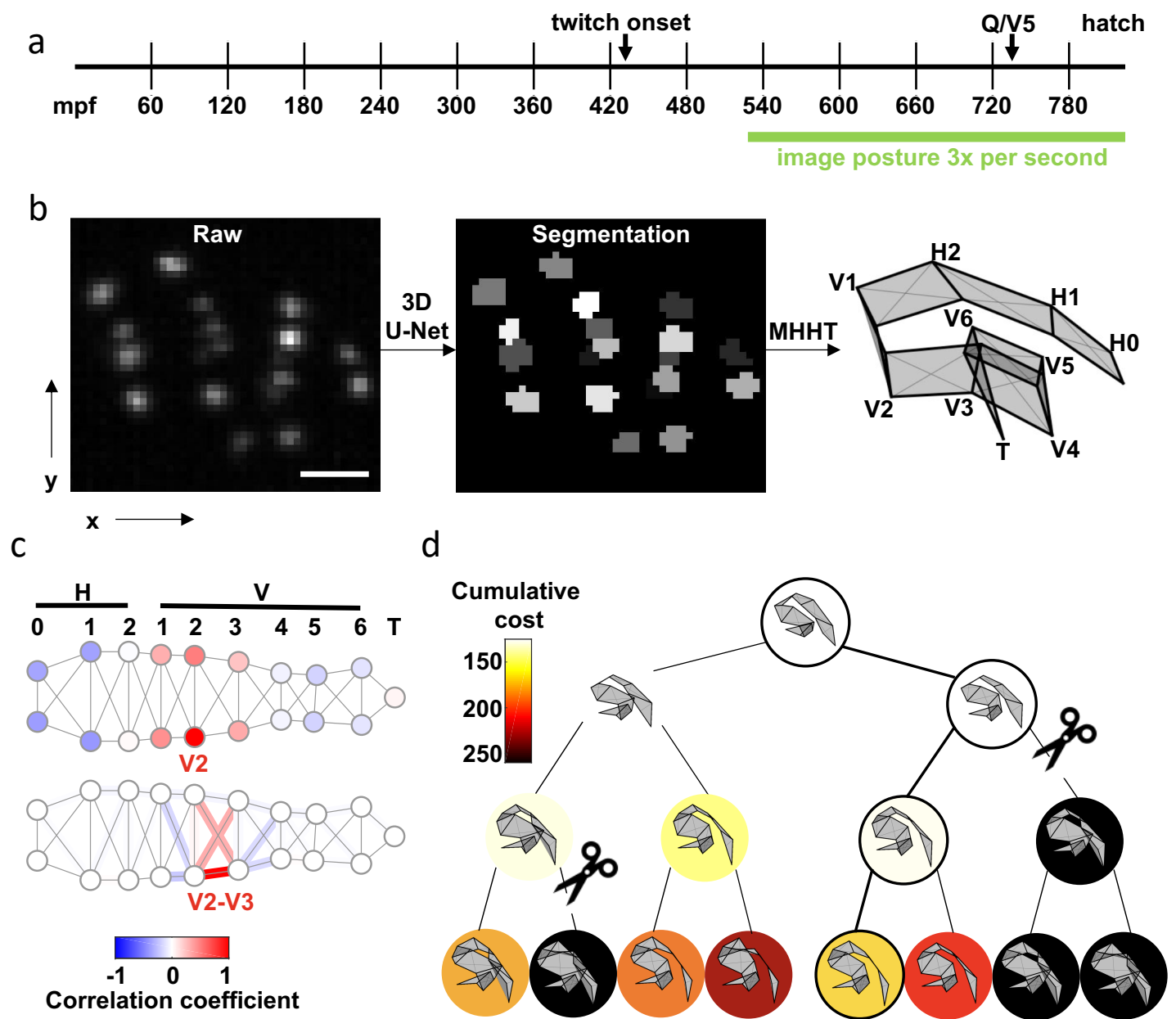[117] M. Weigart, StarDist - Object Detection with Star-convex Shapes, original-date: 2018-06-26T19:54:45Z (Sep. 2021). URL https://github.com/stardist/stardist
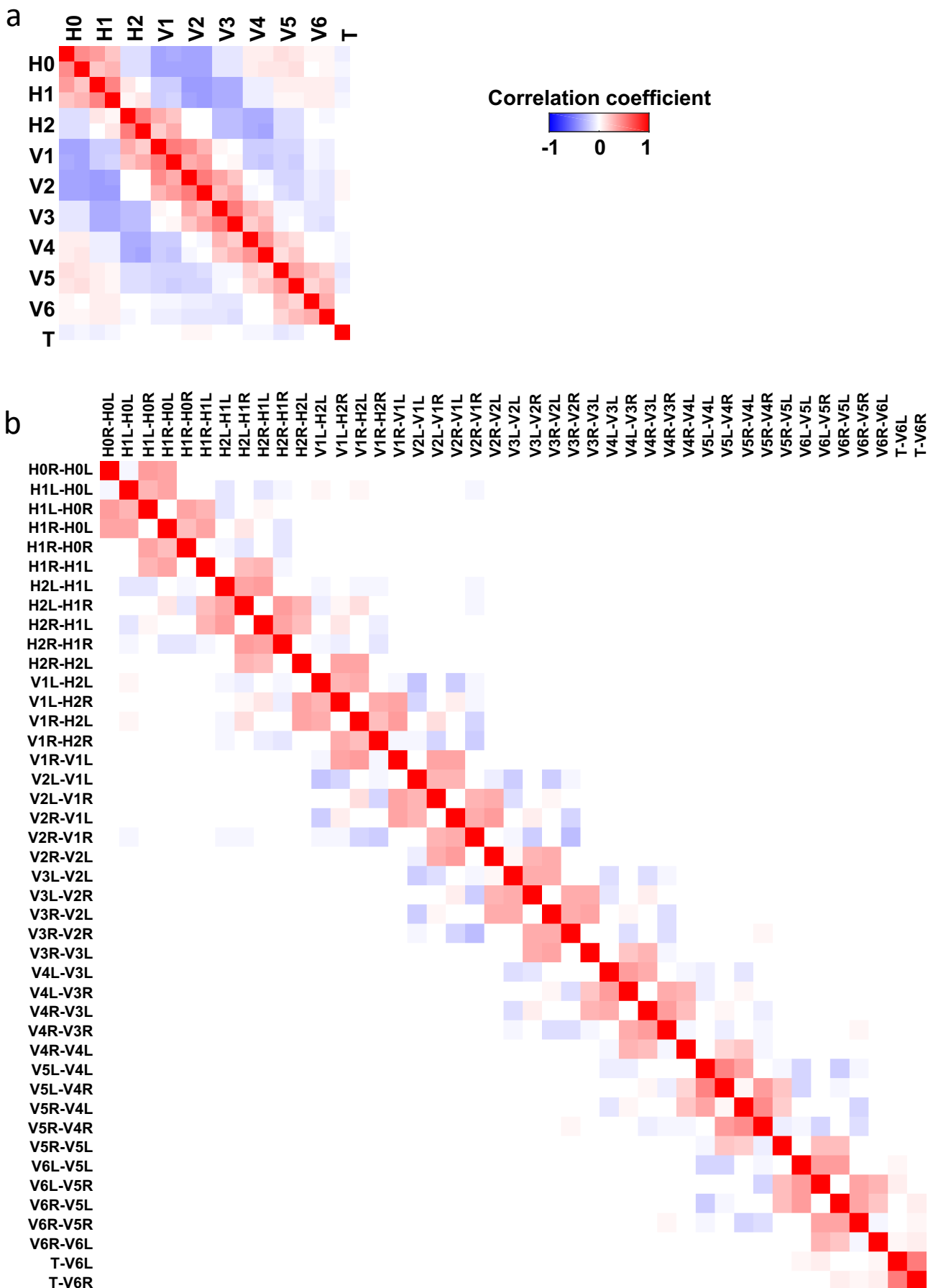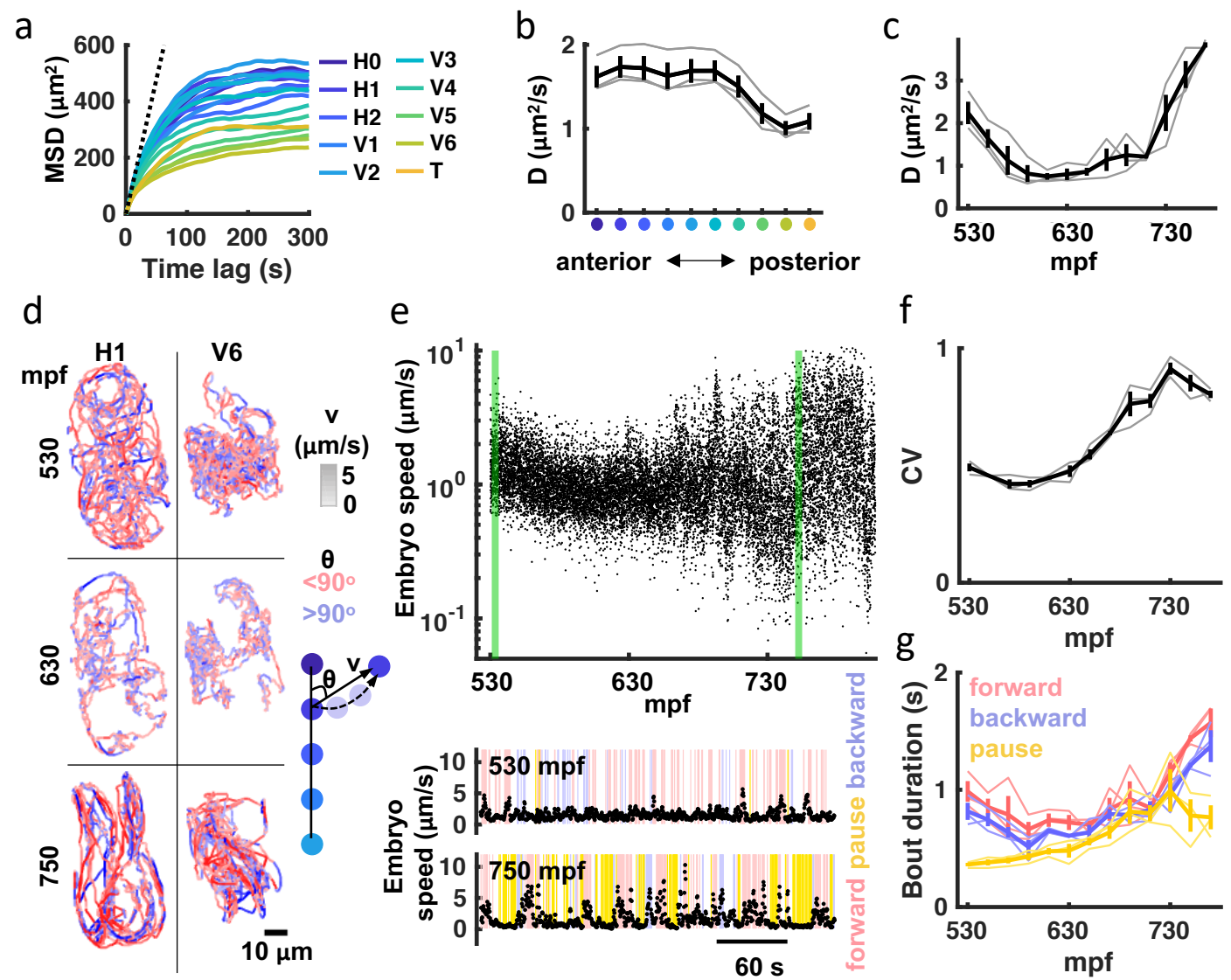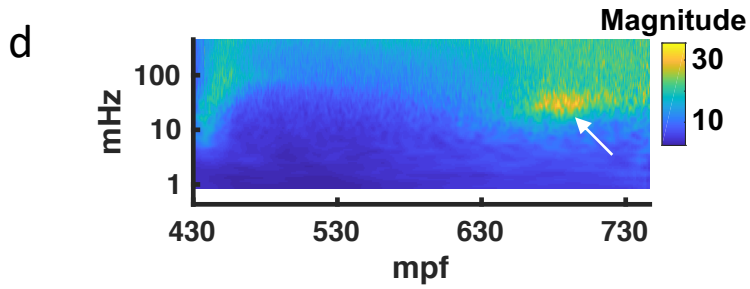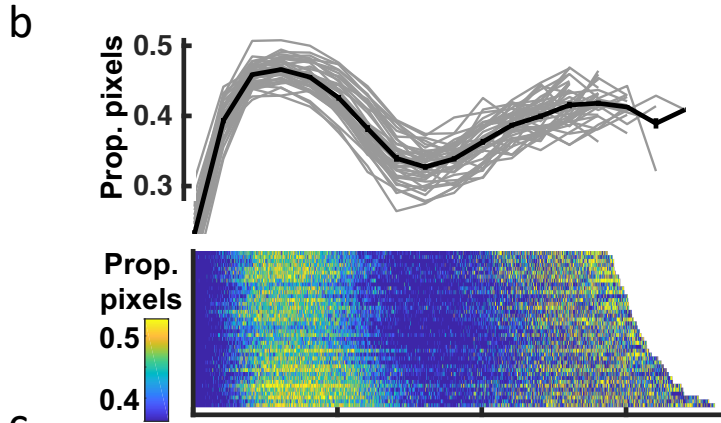
Fig. 1.

Fig. 1-Supp. 1

Fig. 2.

a

b

c

d

Fig. 3.

Fig. 3-Supp. 1

Fig. 4.

a

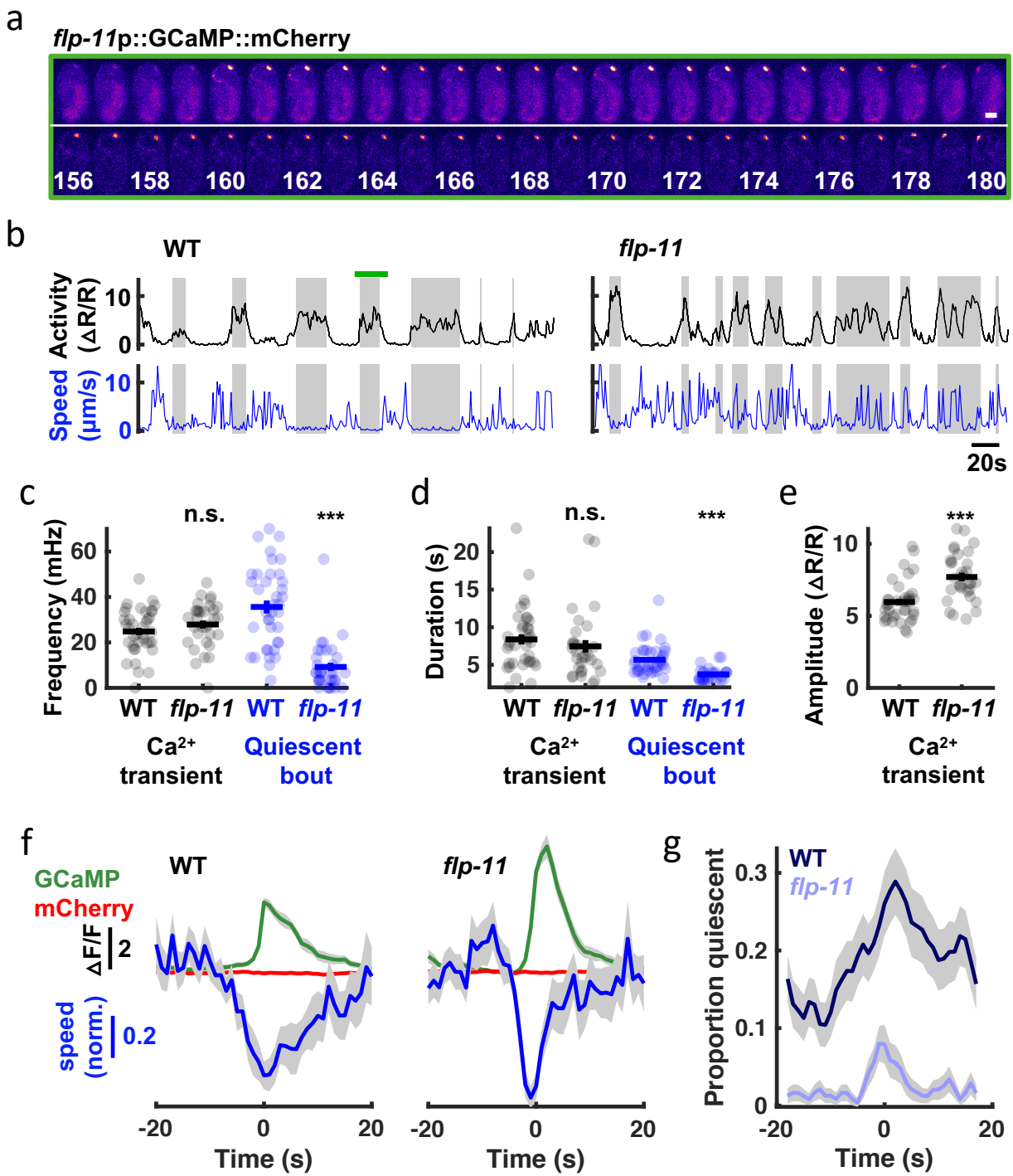**early**
late

150000 postures
3 embryos

Proportion
PC1 amplitude

b

ventral coil   dorsal coil

early
late

992 postures
16 embryos

Proportion
PC1 amplitude

c

DV bend
0
A ↔ P   A ↔ P   A ↔ P   A ↔ P

Fig. 4-Supp. 1

a

530-550 mpf   embryo #1   **750-770 mpf**

PC1

embryo #2

embryo #3

b

530-550 mpf

embryo #1

A
P

embryo #2

A
P

embryo #3

A
P

2 min   -30° V   D 30°

PC3   PC2   PC1

c

750-770 mpf

embryo #1

A
P

embryo #2

A
P

embryo #3

A
P

2 min   -30° V   D 30°

PC3   PC2   PC1

Fig. 4-Supp. 2

a

750 mpf

WT

unc-13

$D\ (\mu m^2/s)$

0 1 2 1 2 3 4 5 6 T
H   V

b

530 mpf

WT

unc-13

$D\ (\mu m^2/s)$

0 1 2 1 2 3 4 5 6 T
H   V

c

Proportion

WT
unc-13

Flip duration (s)

d

WT

unc-13

PC2

PC2

PC3

PC3

PC1

PC1

PC2+
PC2-

PC3+
PC3-

e

PC2

PC1

PC3

ventral
coil

dorsal
coil

intermediates

530 mpf

Fig. 5.

Fig. 6.

Fig. 6-Supp. 1

a

WT

ceh-17

aptf-1(*gk794*)

flp-11

|0.4
60s

**Peak SWT
power ratio**

0   0.2

WT

ceh-17

aptf-1 *gk*   ***

tm   ***

flp-11   ***

b

Prop. pixels

0.4   0.5

WT

flp-11

100
10
1
100
10
1

mHz

Magnitude

30

10

WT

flp-11

530   630   730
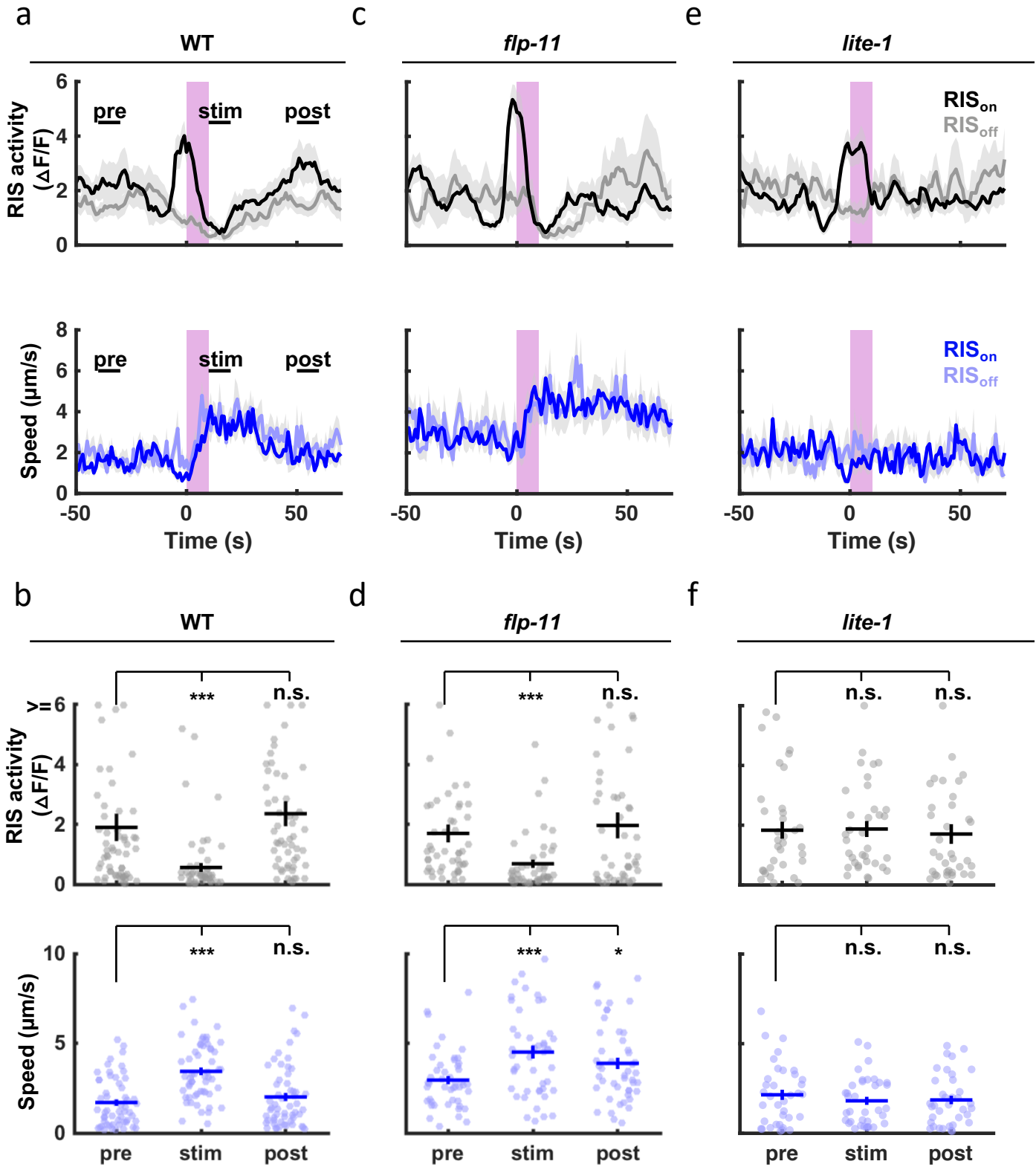
mpf

Fig. 7.

Fig. 7-Supp. 1

a *flp-11*p::GCaMP::mCherry

Fig. 8.

Fig. 8-Supp. 1

Fig. 9.

a

b

Fig. 9-Supp. 1

Fig. 10.